University of Alberta

An Investigation of the Whitecourt Meteorite Impact Crater (Alberta, Canada)

by

Randolf Scott Kofman

A thesis submitted to the Faculty of Graduate Studies and Research
in partial fulfillment of the requirements for the degree of

Master of Science

Earth and Atmospheric Sciences

Spring 2010
Edmonton, Alberta

Examining Committee:

Christopher D. Herd - Earth and Atmospheric Sciences

Duane G. Froese - Earth and Atmospheric Sciences

Douglas R. Schmitt - Physics

Abstract:

The <1,130 year old Whitecourt Meteorite Impact Crater, located several kilometres south of Whitecourt, Alberta (Canada), is a well-preserved bowl-shaped structure having a depth and diameter of ~6 m and 36 m. There are less than a dozen known terrestrial sites of similar size and age. Unlike most of these sites, the Whitecourt Crater contains nearly all the features associated with small impact craters including meteorites, an ejecta blanket, an observable transient crater boundary, a raised rim, and a number of associated shock indicators. The results of this study indicate that the crater formed from the impact of a type IIIAB iron meteorite travelling east-northeast at <10 km/s, striking the surface at an angle between 40° and 55° to horizontal. At present, it appears that the main mass survived atmospheric transit relatively intact to fragment and partially melt during impact, ejecting meteoritic shrapnel, most of which landed downrange.

Acknowledgements:

I would first like to thank James R. and Rodney Stevens, the individuals who recovered the first meteorites associated with the site after concluding that the unusual depression may represent an impact structure. Without them this remarkable crater would continue in obscurity. I would like to thank the Natural Sciences and Engineering Research Council of Canada (NSERC – PGS-M) and The Barringer Crater Company (the Barringer Family Fund for Meteorite Impact Research) for their awards to myself, Discovery Grant 261740 and the Canadian Space Agency (CSA - SSEP CARN) grant to C. D. K. Herd for their generous support for this research project. Matthew Wangler and the Alberta Historical Resources Foundation certainly deserve my gratitude for not only granting the Whitecourt Crater protected status, but also permitting work at the site to continue. I would also like to thank Doug Schmitt, Vadim Kravchinsky, Len Tober, Grey Riddle, Femi Ogunsuyi and Xuefeng Duo (University of Alberta), for their help with several geophysical surveys, training, and for providing equipment. I would also like to thank Marie-Claude Williamson (CSA) for providing an additional magnetometer. For their outstanding work in locating and documenting meteorites at the crater I would like to thank Murray Paulson's volunteer meteorite hunting team consisting of Murray Paulson, Brad Newman, Jen Newman, Rick Huziak and Brian Moore. For helping with my search for shock effects in quartz and general impact dynamics, I would like to thank Christian Koeberl (University of Vienna), Peter Schultz and Scott Harris (Brown University), and Jay Melosh (Purdue University) –a special thanks to Jay Melosh for providing the means to model the impactor's trajectory. For their assistance with sample analysis, I would like to thank George Braybrook, Diane Caird, Sergei Matveev and De-Ann Rollings (University of Alberta). I would also like to thank Laurence Andriashek (Alberta Geological Survey) for sharing his knowledge of the regional geology surrounding the crater and Martin Connors (Athabasca University) for his help investigating the magnetism of the meteorites. Finally I would like to thank Lorne Heibert (Whitecourt Outdoor Ltd.) for his outstanding field support, Brenton Mah and the other field assistants that helped move this work forward, and the people of Whitecourt for not only helping preserve the integrity of the site, but also for the volunteers who spent several days with us searching for meteorites.

Table of Contents:

1. Introduction

1.1. Introduction 1

1.2. Atmospheric Transit Dynamics 2

1.3. Impact Crater 5

1.4. Shock Effects 9

Bibliography 15

2. An Investigation of the Whitecourt Meteorite Impact Crater (Alberta, Canada) 17

2.1 Introduction 17

2.2 Regional Geology 18

2.3 Methods 20

2.4 Results 22

2.4.1 The Impact Crater 22

2.4.2 The Ejecta Blanket 25

2.4.3 The Meteorites 29

2.5 Discussion 34

Bibliography 39

3. Concluding Remarks 44

Bibliography 46

Appendix 47

Appendix 1 – Compositional Analysis of Whitecourt Sediments 47

Appendix 2 – Shock Effects 49

Appendix 3 – Geophysics 55

Appendix 4 – Ballistics 60

Appendix 5 – Impact Parameters 67

Bibliography 75

List of Tables:

Table 1.4.1.	Shock Pressures in Nonporous Rocks	10
Table 1.4.2.	Shock Response of Quartz	13
Table 2.1.1.	Similar Impact Craters	18
Table 3.1.	Summary of Study Results	44
Table A.4.1	Ballistics: Meteorite Properties	63
Table A.4.2	Ballistics: Results	64
Table A.5.1	Modeling: Results	70

List of Figures:

Figure 1.1.1	LiDAR Images of the Site	2
Figure 1.2.1	Mayerthorpe Meteorite	3
Figure 1.2.2	Bow Shock Interaction	5
Figure 1.2.3	Sikhote Alin Strewn Field	5
Figure 1.3.1	Stages of Crater Formation	7
Figure 1.3.2	Cross-section of an Ideal Simple Crater	8
Figure 1.4.1	PDF-Bearing Quartz Samples	12
Figure 2.2.1	Local Soil Profile	20
Figure 2.3.1	Auger Sample Chamber with Paleosol	21
Figure 2.4.1	LiDAR Image of Crater with Surface Contours	23
Figure 2.4.2	Cross-section of Crater and Sediments	24
Figure 2.4.3	SEM Image of Fe-Ni Oxide Spherule	25
Figure 2.4.4	Proximal Ejecta	26
Figure 2.4.5	Cross-Sections of Ejecta Blanket	27
Figure 2.4.6	Proximal, Medial and Distal Ejecta	28
Figure 2.4.7	Meteorite Samples	30
Figure 2.4.8	Meteorite Mass Distribution	31
Figure 2.4.9	Shale Ball Sample	33
Figure 2.4.10	Magnetic Survey Results	34
Figure 2.5.1	Summary Diagram	35
Figure A.1.1	XRD Analyses of Sand(stone) Results	47
Figure A.1.2	Locations of Outcrops	48
Figure A.2.1	HF Etching Apparatus	51
Figure A.2.2	Fe-Ni Oxide Spherule and Meteorite Dust Samples	51
Figure A.2.3	PM-Bearing Quartz Samples	52
Figure A.2.4	SEM Image of Etched Quartz Grain	53
Figure A.3.1	ERT Survey Results	56
Figure A.3.2	Magnetic Survey Results	57
Figure A.3.3	Meteorite Remnant Magnetic Field Measurements	57
Figure A.4.1	Plot of Drag Coefficient Vs Reynolds Number	62
Figure A.4.2	Ballistics: Results	65

Chapter 1: Introduction

1.1 Introduction

The Whitecourt Meteorite Impact Crater was discovered in July 2007 after two residents of the Whitecourt and Mayerthorpe area of Alberta brought it to the attention of Dr. Christopher Herd. A number of locals had been aware of the unusual depression for over a decade though it was the discovery of meteorites at the site by James R. Stevens and Rodney Stevens that inspired them to seek out confirmation of its impact origin. A visit to the site and subsequent analysis of the meteorites removed any doubt as to the impact origin of the structure. The origin of the Whitecourt Crater, based on field and laboratory observations and complemented by modeling, forms the basis of this study.

The Whitecourt Crater is remarkable for several reasons. The crater's age (<1.13 ka [Herd *et al.* 2008]), diameter (36 m), and associated meteorites make it the youngest, smallest, and only crater with associated meteorites in Canada. Additionally, the Whitecourt Crater is one of the most well preserved terrestrial impact structures, particularly among structures of similar dimensions. As such, it provides a significant new data source for the study of impact related processes.

An aerial view of the crater and surrounding area illustrates the obscuring effects of vegetation for a structure this size (Figure 1.1.1A). The LiDAR data (**Li**ght **D**etection **A**nd **R**anging) used to generate these images is capable of removing vegetation to expose the surface, making the Whitecourt Crater visible (Figure 1.1.1B). These data provide an essential foundation for the study by providing not only a clear view of the site, but also a digital elevation model on which subsequent data can be overlain. Consequently, LiDAR imaging provides an excellent tool for detecting and studying small terrestrial impact craters [Herd *et al.*, 2008].

The primary goals of this research project are to determine the morphology and stratigraphy of the crater and the surrounding sediments, determine the distribution of the associated meteorites and ejecta, and constrain the pre-impact and impact parameters. A combination of geological, geophysical and geochemical methods applied to the site, the sediments and the meteorites will make this possible. As the sole investigators of this site, we have the privilege of introducing this crater to the world.

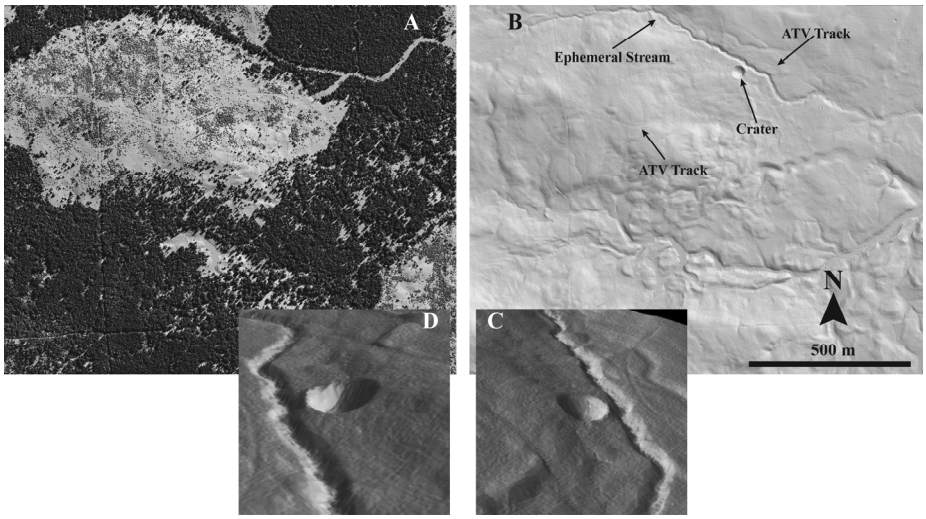

Figure 1.1.1: Full-feature (A) and bare-Earth (B) LiDAR images of the crater and surrounding area and an oblique view looking northwest (C) and southeast (D) of the crater from a LiDAR-derived DEM.

Chapter 2 and the subsequent appendices in this thesis summarize the results of the study. The following brief reviews of three major aspects of the impact process provide some of the background information necessary for the reader to understand the observations and interpretations made at the site. The key aspects include the atmospheric transit of the incoming meteoroid, the cratering process and the most common shock effects related to these energetic events.

1.2 Atmospheric Transit Dynamics

One of the most significant differences between impact events on Earth and those on most other rocky bodies in the Solar System is the presence of an atmosphere. The Earth's atmosphere acts as a filter that affects many of the variables involved in impact events. Three important terms relating to the incoming projectile include (1) meteoroid, which refers to the projectile prior to entering the Earth's atmosphere, (2) meteor, which refers to the atmospheric phenomenon of the projectile traveling through Earth's atmosphere, and (3) meteorite, which refers to a projectile that has come to rest on Earth's surface. The level of atmospheric influence, controlled by the incoming meteoroid's mass, shape, velocity, impact angle, and competence determine how much time the meteoroid will spend in the atmosphere and how strongly it will respond to atmospheric interaction. Iron meteoroids represent the most competent and dense objects striking the atmosphere and therefore stand the greatest chance of reaching the surface intact.

Meteoroids typically strike the tenuous upper atmosphere with average velocities of ~20 km/s and at an angle 45° to the surface of Earth [Melosh, 1989]. At such high velocities, the density of the lower atmosphere can have devastating effects on the incoming meteoroid. This typically results in ablation and fragmentation of the meteoroid while it traverses the atmosphere. When the velocity of the meteoroid exceeds a material specific critical velocity, V_{crit}, ablation occurs. At sea level V_{crit} is ~3.0 km/s for steel and would be a similar value for an iron meteorite [Allen *et al.,* 1952; Passey & Melosh, 1980]. At the lowest velocities, ablation results in a thin veneer of molten material that encapsulates the meteoroid, which, upon slowing and cooling, quenches to form a fusion crust. At higher velocities, ablation may lead to the formation of regmaglypts and significant mass loss as ablation removes material from the surface of incoming meteor (Figure 1.2.1).

Figure 1.2.1: A sample of the Mayerthorpe iron meteorite with a dark fusion crust and regmaglypts. Regmaglypts are the thumbprint-like depressions covering the surface of the meteorite. Photograph by Andrew Locock, University of Alberta.

Fragmentation events represent the most dynamic atmospheric phenomena experienced by incoming meteoroids. Fragmentation occurs in response to pressure build-up along the leading edge of the meteor because of its hypersonic transit through the atmosphere. At hypersonic speeds, a bow shock will develop immediately preceding the meteor (Figure 1.2.2). In the standoff zone between the bow shock and the leading edge of the meteor the stagnation pressure, P, is defined as:

$$P = \rho_a V^2$$

where ρ_a is the mass density of the atmosphere and V is the velocity of the meteoroid. The pressure behind the meteoroid is essentially zero. Once the stagnation pressure increases beyond the crushing strength of the meteoroid, it fragments catastrophically. This typically results in a small number of large fragments and a large number of small

fragments [Passey & Melosh, 1980]. It is worth noting that the actual pressure required for catastrophic disruption can be more than an order of magnitude lower than the measured mechanical strength of recovered meteorite fragments [e.g. Petrovic, 2001] and is, in part, controlled by the rate at which the pressure changes (i.e. the steepness of the meteoroid's trajectory) [e.g. Forschini, 2001; Kenkmann *et al.*, 2009]. Fragmentation events typically occur at altitudes of 4 km to 40 km [Passey & Melosh, 1980].

Fragmentation events not only break up the main body of the incoming meteoroid, they also lead to the dispersion and deceleration of the resultant fragments. Figure 1.2.2 illustrates bow shock interaction, one of the processes responsible for both dispersion and deceleration. If the fragments reach Earth's surface for significantly oblique impact trajectories, they will typically be scattered across an elliptical area called a strewn field, or scatter ellipse (Figure 1.2.3). The long axis of the strewn field will delineate the original meteoroid's trajectory with the smaller fragments concentrated uprange and the larger fragments, and possible impact structures, concentrated downrange. The research and development of atmospheric transit models is continually improving our ability to predict the results of a variety of transit scenarios. Examples of two simplified models that account for catastrophic disruption include the pancake model [Chyba *et al.* 1993], and the separated fragments model [Passey & Melosh, 1980; Artemieva & Shuvalov 1996, 2001].

Ablation and fragmentation can affect meteoroids of all sizes. However, smaller meteoroids (which are mechanically stronger than larger meteoroids of the same type [Weibull, 1951]), slower meteoroids, more competent meteoroids, and meteoroids entering Earth's atmosphere at shallow angles are more likely to survive transit intact [e.g. Kenkmann *et al.* 2009]. Meteoroids larger than a kilometre in diameter essentially do not 'see' the atmosphere and, therefore, strike the surface at their full cosmic velocity and with an unaltered trajectory [Passey & Melosh, 1980; Melosh, 1989].

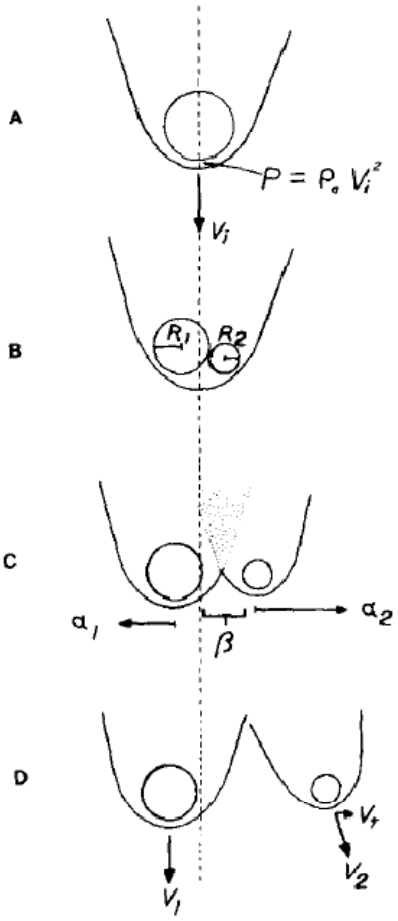

Figure 1.2.2: A schematic diagram illustrating the effects of bow shock interaction. Captions A to D represent increasing time. The diagram shows how the interaction of different bow shocks developed following a fragmentation event can lead to transverse accelerations (α_1 and α_2) causing fragments to separate. At stage D the bow shocks no longer interact. V_i is the initial velocity while V_1 and V_2 are the final modified velocities [Passey & Melosh, 1980].

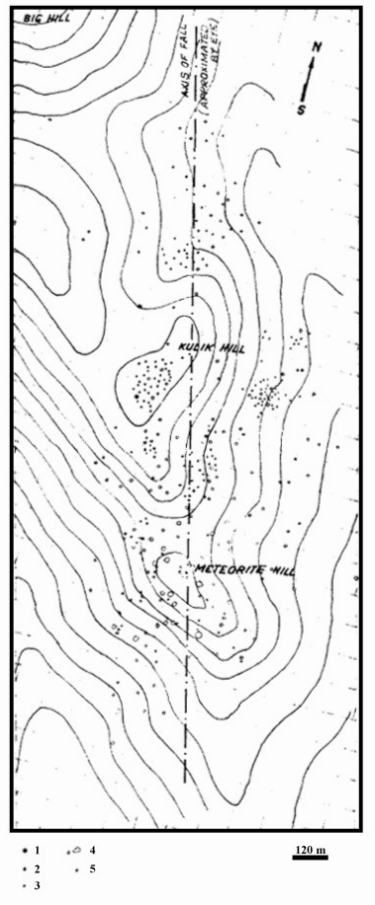

Figure 1.2.3: Diagram of the Sikhote Alin strewn field. The impactor flight direction was roughly North to South. (1) meteorites with mass between 10 to 100 kg; (2) meteorites with mass between 1 to 10 kg; (3) meteorites with mass less than 1 kg; (4) craters with diameter between 5 to 28 m; (5) craters with diameter less than 5 m [Lang & Kowalski, 1973]. This strewn field resulted from several successive fragmentation events. Note that the impact structures are concentrated downrange.

1.3 Impact Craters

Impact craters are classified according to their size and structure. There are three major classes of craters: simple, complex and multi-ring basins [French, 1998]. Simple craters represent the smallest explosive craters and on Earth are typically less than about four kilometres in diameter; the actual diameter at which a crater transitions from simple to complex to multi-ringed depends primarily on the properties of the target rock and the

target's gravitational field. An ideal simple crater consists of a circular bowl-shaped, breccia-filled depression with an uplifted rim surrounded by ejecta (Figure 1.3.1f). Complex craters have varying morphologies depending on their diameter. As the diameter of complex craters increases they transition from central-peak to central-peak-basin structures and finally to peak-ring basin structures before becoming multi-ring basins [French, 1998; Melosh, 1989]. The following discussion will focus on simple craters, which are analogous to the Whitecourt Crater.

The formation of a simple crater can be broken down into three stages: (1) contact and compression, (2) excavation and (3) modification. Unless otherwise stated the descriptions of these stages, shown in Figure 1.3.1, represent a brief summary of the stages described by French (1998). The contact and compression stage begins when the impactor strikes the target surface. This generates a shock wave that travels simultaneously downward into the ground and upward through the impactor towards its trailing edge. Both the impactor and the target material are compressed. Once the shock (compression) wave reaches the rear of the impactor it reflects as a rarefaction (tensional) wave, the pressure unloading of the impactor causes it to fragment and/or convert, virtually instantaneously, into melt or vapor depending on the velocity and strength of the impactor. It is important to note that, in general, extensive melting of target material typically does not occur below impact velocities of 12 km/s [O'Keefe & Ahrens 1982b]. Once the rarefaction wave reaches the leading edge of the impactor and enters the compressed target material the contact and compression stage ends and the excavation stage begins. For most impacts, the duration of this stage is only a fraction of a second [Melosh, 1989].

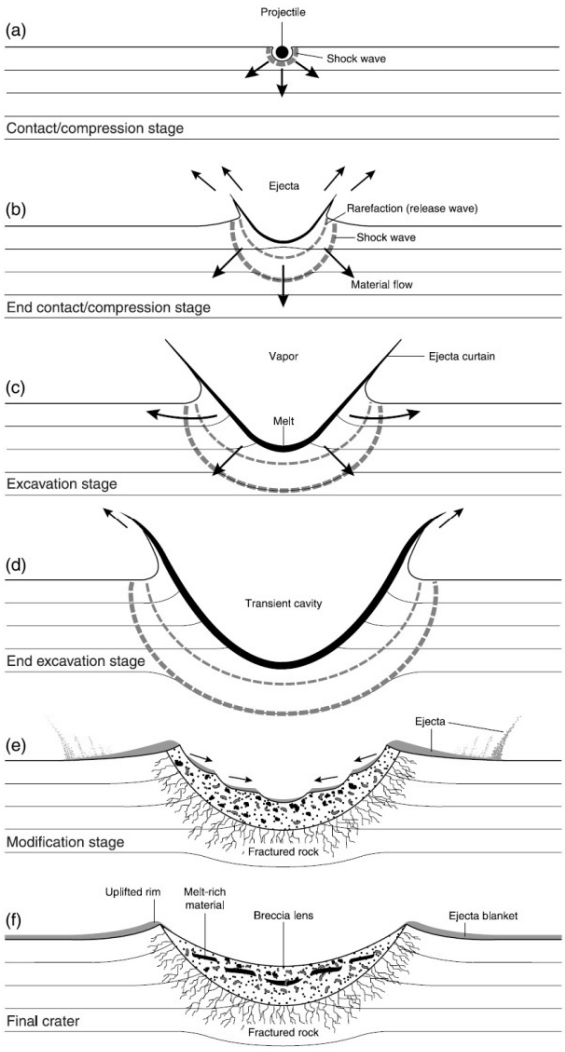

Figure 1.3.1: Cross-sectional views of the different stages of formation of a simple crater [French, 1998].

It is during the excavation stage that the formation of an unmodified bowl-shaped depression, or transient crater, occurs. The crater's excavation results from the interactions between the expanding shock waves and the original target surface. This process leads to three different excavation flow regimes initiated by the impact-generated shock wave. The near-surface regime, where weakly shocked material spalls off the surface at high velocities (Figure 1.3.2), forms in response to the interaction of the shock waves travelling upward towards the surface and the reflected rarefaction waves travelling downward from the surface-atmosphere interface. In the flow regime between the surface and the excavation depth, H_{exc}, the dominant flow is outward and upward primarily in response to the initial shock wave. The sediments within the first two flow

regimes constitute the material ejected from the crater. In the deepest flow regime, at depths below H_{exc}, material flow is outward and downward, which results in a bowl-shaped depression. The outward motion in the deepest flow regime also contributes to the structurally uplifted rims that are typical of simple craters. In an unconsolidated sedimentary target, the shock and rarefaction waves dissipate quickly. Once particle motion slows and the flow field is no longer capable of excavating, or displacing material, the maximum dimensions of the transient crater are reached. At this point, the excavation stage ends and the modification stage begins. The excavation stage is rapid, requiring only about six seconds for a 1 km diameter crater as has been determined for Meteor Crater in Arizona [Melosh, 1989].

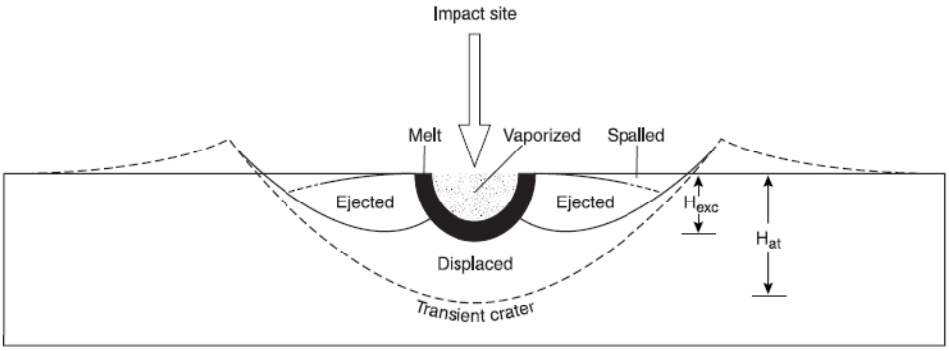

Figure 1.3.2: This theoretical cross-section through a transient crater indicates the response of the target material to the impact during the excavation stage. The vaporized impactor and target material expands outward and upward as a vapor plume. The melted impactor/target material expands outward and downward towards the transient crater boundary. The ejected target material expands upward and outward towards and beyond the transient crater rim. The displaced target material expands downward and outward towards the transient crater boundary forming the parautochthonous rocks below the transient crater. $\mathbf{H_{at}}$ is the final depth of the transient crater. $\mathbf{H_{exc}}$ is the depth to which material is excavated [Melosh, 1989].

The shock and rarefaction waves play no part in the modification stage, which is controlled by gravity and rock/sediment mechanics. The main event of the modification stage for simple structures is the collapse of the material along the transient crater walls, infilling the transient crater and forming the allochthonous breccia lining the crater floor. The bulk of the modification stage ends quite literally when 'the dust settles,' though erosion, isostatic rebound and other more typical geologic processes may continue for long periods following the event. During this process, the diameter of the crater will increase as the transient crater walls collapse to an appropriate angle of repose, and the depth of the crater will decrease as the material settles along the base. This results in the observed diameter and depth.

Several variables control the final crater morphology. The impactor's mass, velocity, diameter, density, and impact angle at the time of the collision are among the most important. The impact angle affects the size and shape of the crater, and the distribution of the ejecta blanket (the area surrounding the crater covered continuously by ejecta). To a large extent the impact angle, or more specifically the angle at which the impactor enters the atmosphere, also controls the distribution of the meteorites that strike outside the crater, forming the strewn field – assuming that meteorites are present and resulted from atmospheric disruption, not material that spalled off the impactor when it struck the surface. The mass, velocity, diameter and density (both pre- and post-atmospheric), in addition to the properties of the target surface, control the size of the crater. This study will place some constraints on these variables with regard to the Whitecourt Crater.

1.4 Shock Effects

Due to the active geological processes on Earth, terrestrial impact craters are often in a heavily weathered state when discovered. As such, impact structures often have questionable origins. In many cases surviving shock-metamorphic effects provide critical evidence of impact origin. The following paragraphs, outlining shock-metamorphic effects in general, represent a summary of the effects described by French (1998).

Shock-metamorphic effects arise from pressures and strain-rates much higher than typical surface geological processes. In any given impact event, peak shock pressures may range from ≤2 GPa near the crater rim to ≥100 GPa near the point of impact. In most geologic settings, similar pressures generally reflect static conditions at depths of 75 km to 1000 km beneath Earth's surface. Shock pressures generated during impact are both brief and intense in the application and release of the induced high-pressure wave. In addition to the transient stress conditions, high strain-rates ($>10^{-5}$ s^{-1} [Grieve *et al.* 1996]), and rapid quenching, shock waves also deposit energy into the materials through which they pass. In particular, specific shock-pressures will result in specific post-shock temperatures depending on the nature of the target materials (greater pressure implies greater temperatures – Table 1.4.1). With increasing shock pressure, the effects will extend beyond deformation and melting or vaporization may occur. The final

state of the shocked materials results from the shock compression and release, and subsequent post shock temperatures.

There are a number of different shock-effects produced during an impact event. In addition to providing a shock-barometer indicating the pressures that existed during the event, some of these effects are produced only during impact events. Table 1.4.1 shows an example of the general progression of shock-effects with increasing pressure and post-shock temperature *for crystalline targets*.

Table 1.4.1: A summary of shock pressure effects in *nonporous* target rocks [French, 1998].

Approximate Shock Pressure (GPa)	Estimated Post-Shock Temperature (°C)*	Effects
2 - 6	<100	Rock fracturing; breccia formation shatter cones
5 - 7	100	Mineral fracturing: {0001} and {$10\bar{1}1$} in quartz
8 - 10	100	Basal brazil twins {0001}
10	100*	Quartz with PDFs {$10\bar{1}3$}
12 - 15	150	Quartz → stishovite
13	150	Graphite → cubic diamond
20	170*	Quartz with PDFs {$10\bar{1}2$}, etc. quartz, feldspar with reduced refractive indexes, lowered birefringence
>30	275	Quartz → coesite
35	300	Diaplectic quartz & feldspar glasses
45	900	Normal (melted) feldspar glass (vesiculated)
60	>1,500	Rock glasses, crystallized melt rocks (quenched from liquids)
80 - 100	>2,500	Rock glasses (condensed from vapor)

* For dense nonporous rocks. For porous rocks (e.g., sandstones), postshock temperatures = 700°C (P = 10 GPa) and 1560°C (P = 20 GPa). Data from Stöffler (1984); Melosh (1989) and Stöffler & Langenhorst (1994).

The relatively well-understood distribution of shock pressures in crystalline targets can provide a means of reconstructing the target surface at the instant of impact with the various pressure regimes restored to their initial positions – prior to subsequent transport and excavation as part of the crater forming process. In an unconsolidated target, such as at the Whitecourt Crater, the pressure distribution is much more heterogeneous, particularly on a microscopic scale. In addition, it is expected that the melting of target material of a specific composition will occur at lower temperatures in a

porous medium relative to a non-porous medium and that some features, such as high-pressure polymorphs, will form at lower overall pressures.

As the identification of shock-effects is one objective of the study at the Whitecourt Crater, the inclusion of brief descriptions and, where useful, representative images are necessary. Shatter cones will not be addressed as they cannot develop in unconsolidated materials [e.g. Kenkmann *et al.* 2009]. The following descriptions represent a summary of the features provided by Grieve *et al.* (1996).

Mosaicism: Shock-induced mosaicism appears under optical microscopy as a highly irregular mottled extinction pattern in quartz with domains typically >200 nm. The domain size decreases with increasing pressure. Mosaicism may, or may not coexist with planar microstructures.

Planar microstructures: While planar microstructures may form in a variety of minerals, the following discussion will be restricted to quartz, which is more relevant to the Whitecourt Crater. The mechanical failure in quartz occurs in two forms: first through the development of irregular fractures, which are not diagnostic, and second by the development of regular planar microstructures. Planar microstructures are diagnostic and are oriented parallel to rational crystallographic planes having low Miller indices. The two main types of planar microstructures are planar fractures (PFs) and planar deformation features (PDFs). Planar fractures typically occur as parallel cracks along {0001} and $\{10\bar{1}1\}$ having a spacing ≥20 μm. Planar deformation features typically occur as multiple sets (1 to 15 sets may be present in a single grain) of parallel, planar lamellae, typically 2 to 10 μm apart, which are often resolvable using optical microscopy. PDF's may appear as fresh amorphous lamellae 30 nm to 200 nm thick (Figure 1.4.1A) or as planes decorated with tiny vugs as is the case for decorated PDFs (Figure 1.4.1B). The most common orientations for PDFs are: $\{10\bar{1}3\}$, $\{10\bar{1}2\}$, $\{10\bar{1}1\}$, {0001}, $\{11\bar{2}1\}$, $\{11\bar{2}2\}$, $\{21\bar{3}1\}$, $\{22\bar{4}1\}$, $\{51\bar{6}1\}$, $\{10\bar{1}0\}$ and $\{11\bar{2}0\}$. Basal PDFs, those along {0001}, represent multiple mechanical Brazil twin lamellae and, unless decorated, are not typically visible using optical microscopy.

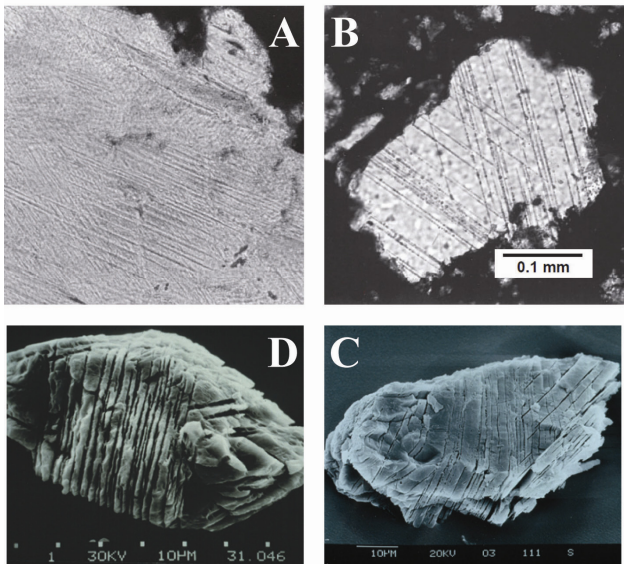

Figure 1.4.1: Examples of PDFs in quartz. (A) Photomicrograph (cross-polarized light) showing multiple sets of 'fresh' PDFs formed at pressure >15 GPa in a sample from the Lake St. Martin impact structure in Manitoba (Canada) [French, 1998]. Note the dark patches of diaplectic glass along the top right of the image. (B) Two sets of partially decorated PDFs from Gardnos (Norway) (plane-polarized light) [French, 1998]. (C) From the Deep Sea Drilling Project site 596 and (D) from Brownie Butte, Montana (U.S.A), are SEM images of PDF-containing quartz grains etched using hydrofluoric acid. (C) and (D) are images by B. Bohor, USGS, provided by C. Koeberl, University of Vienna.

Diaplectic Glass: Once shock pressures increase to the point of developing PDFs along $\{10\bar{1}3\}$ and $\{10\bar{1}2\}$ (Table 1.4.2 – Grieve *et al.* 1996) the refractive indices and birefringence of quartz gradually decrease until it becomes isotropic – i.e. it has become diaplectic glass. The morphology of the quartz grain will not change during the transformation and there will be no evidence of fluid textures (Figure 1.4.1A).

Coesite and Stishovite: These high-pressure quartz polymorphs occur as very fine-grained aggregates formed by the partial transformation of the host grain. At Meteor Crater, Arizona, coesite grains are typically 5 µm to 50 µm in diameter [Chao *et al.* 1960] and stishovite grains all sub-micrometre [Chao *et al.* 1962]. The conditions required for development of coesite and stishovite vary significantly between non-porous and porous media. In porous sandstone, more analogous to the target materials at the Whitecourt Crater, coesite forms at average shock pressures estimated between 5 GPa and 10 GPa and coexists with >80 % of quartz grains containing PDFs and diaplectic quartz glass. At shock pressures of ~13 GPa to 30 GPa an assemblage of fractured and amorphous quartz, coesite and stishovite is observed [Kieffer, 1971; Kieffer *et al.* 1976]. These pressures are significantly lower than required in non-porous media: 30 GPa to 60 GPa and 12 GPa to 45 GPa for coesite and stishovite formation respectively.

Table 1.4.2: Qualitative summary of the reponse of quartz to various shock regimes in non-porous target materials [Grieve *et al.* 1996].

Shock stage	Critical sets of PFs and PDFs*	Additional sets of PFs and PDFs	Optical properties of quartz
(1) Very weakly shocked	PFs: PDFs: (0001)	PFs: {10$\bar{1}$1} rare PDFs: none	Normal
(2) Weakly shocked	PDFs: {10$\bar{1}$3}	PFs: {10$\bar{1}$1} , (0001) PDFs: (0001)	Normal
(3) Moderately shocked	PDFs: {10$\bar{1}$3}	PFs: {10$\bar{1}$1} , (0001) rare PDFs: {11$\bar{2}$1} , {11$\bar{2}$2} , (0001), {10$\bar{1}$0} + {11$\bar{2}$1} , {10$\bar{1}$1} , {21$\bar{3}$1} , {51$\bar{6}$1}	Normal or slightly reduced refractive indices
(4) Strongly shocked	PDFs: {10$\bar{1}$2} , {10$\bar{1}$3}	PFs: rare or absent PDFs: {11$\bar{2}$1} , {11$\bar{2}$2} , (0001), {10$\bar{1}$0} + {11$\bar{2}$1} , {10$\bar{1}$1} , {21$\bar{3}$1} , {51$\bar{6}$1}	Reduced refractive indices: 1.546–1.480
(5) Very strongly shocked	PDFs: {10$\bar{1}$2} , {10$\bar{1}$3}	rare	Reduced refractive indices: <1.480
(6) Extremely shocked			Diaplectic glass, refractive index: 1.468–1.461
(7) Shock fused			Lechatelierite, refractive index: 1.460–1.458

* The shock metamorphic stages observed in quartz found in *non-porous* rocks, modified from Stöffler and Langenhorst (1994).

Lechatelierite (fused silica glass): Lechatelierite forms a highly vesiculated glass containing flow structures. Lechatelierite occurs most commonly in target materials composed of sedimentary rocks or unconsolidated sediments and frequently coexists with less shocked crystalline quartz and coesite. Lechatelierite is one of the products of the highest degrees of shock (Table 1.4.2 [Grieve *et al.* 1996]).

Spherules [French, 1998]*:* Glassy spherules form in response to the rapid cooling of shock-melted droplets of target and/or impactor materials. These μm- to mm-scale objects are typically concentrated in the most distal ejecta deposits and surrounding surface sediments. However, the nature of spherules makes them susceptible to weathering and erosion, which may explain why they are not always observed at impact craters. (e.g. Krinov, 1966; Mittlefehldt et al.1992).

Tektites and Microtektites [French, 1998]*:* Tektites (cm-scale) and microtektites (≤1 mm) are glassy objects that are typically black, though they may be greenish, brownish, or grayish in color. The current consensus is that these glassy objects represent melt ejected during impact events. Tektites and microtektites are completely glassy lacking any microlites or phenocrysts and have a chemical and isotopic composition

similar to shales and other sedimentary rocks. They may contain shocked mineral grains, high-pressure polymorphs (e.g. coesite), Lechatelierite, or in rare cases, the chemical signature of an extraterrestrial impactor. Similar to meteorites, tektites and microtektites are often distributed throughout a strewn field related to their origin. [See reviews by O'Keefe, 1994; 1990; Koeberl, 1986, 1994a].

Bibliography

Allen, W. A., Rinehart, J. S., & White, W. C. (1952). Phenomena Associated with the Flight of Ultra-Speed Pellets, Part I. Ballistics. *Journal of Applied Physics, 23*, 132-137.

Artemieva, N., & Shuvalov, V. (1996). Interaction of Shock Waves During the Passage of a Disrupted Meteoroid Through the Atmosphere. *Shock Waves, 5*, 359-367.

Artemieva, N., & Shuvalov, V. (2001). Motion of a Fragmented Meteoroid Through the Planetary Atmosphere. *Journal of Geophysical Research, 106*, 3297-3309.

Chao, E. C., Fahey, J. J., Littler, J., & Milton, D. J. (1962). Stishovite, SiO_2, a very High Pressure new Mineral from Meteor Crater, Arizona. *Journal of Geophysical Research, 67*, 419-421.

Chao, E. C., Shoemaker, E. M., & Madsen, B. M. (1960). First Natural Occurence of Coesite. *Science, 132*, 220-222.

Chyba, C. F., Thomas, P. J., & Zahnle, K. J. (1993). The 1908 Tunguska explosion: Atmospheric disruption of a stony asteroid. *Nature, 361*, 40-44.

Foschini, L. (2001). On the Atmospheric Fragmentation of Small Asteroids. *Astronomy & Astrophysics, 365*, 612-621.

French, B. M. (1998). *Traces of Catastophe: A Handbook of Shock-Metamorphic Effects in Terrestrial Meteorite Impact Structures.* LPI Contribution No. 954, Lunar and Planetary Institute, Houston. 120 pp.

Grieve, R. A., Langenhorst, F., & Stöffler, D. (1996). Shock Metamorphism of Quartz in Nature and Experiment: II. Significance in Geoscience. *Meteoritics & Planetary Science, 31*, 6-35.

Herd, C. D., Froese, D. G., Walton, E. L., Kofman, R. S., Herd, E. P., & Duke, M. J. (2008). Anatomy of a Young Impact Event in Central Alberta: Prospects for the 'Missing' Holocene Impact Record. *Geology, 36* (12), 955-958.

Kenkmann, T., Artemieva, N. A., Wünnemann, K., Poelchau, M. H., Elbeshausen, D., & Núñez del Prado, H. (2009). The Carancas Meteorite Impact Crater, Peru: Geologic Surveying and Modeling of Crater Formation and Atmospheric Passage. *Meteoritics & Planetary Science, 44* (7), 985-1000.

Kieffer, S. W. (1971). Shock Metamorphism of the Coconino Sandstone at Meteor Crater, Arizona. *Journal of Geophysical Research, 76*, 5449-5473.

Kieffer, S. W., Phakey, P. P., & Christie, J. M. (1976). Shock Processes in Porous Quartzite: Transmission Electron Microscope Observations and Theory. *Contributions to Mineralogy and Petrology, 59*, 41-93.

Koeberl, C. (1986). Geochemistry of Tektites and Impact Glasses. *Annual Review of Earth and Planetary Sciences, 14*, 323-350.

Koeberl, C. (1994a). Tektite Origin by Hypervelocity Asteroidal or Cometary Impact: Target Rocks, Source Craers, and Mechanisms. In B. O. Dressler, A. F. Grieve, & V. L. Sharpton (Eds.), *Large Meteorite Impacts and Planetary Evolution* (pp. 133-151). Geological Society of America Special Paper 293.

Krinov, E. L. (1966). *Giant Meteorites* (1st english ed.). New York: Pergamon Press.

Melosh, H. J. (1989). *Impact Cratering : A Geologic Process.* New York: Oxford University Press.

Mittlefehldt, D. W., See, T. H., & Hörz, F. (1992). Dissemination and Fractionation of Projectile Materials in the Impact Melts from Wabar Crater, Saudi Arabia. *Meteoritics and Planetary Science, 27*, 361-370.

O'Keefe, J. A. (1994). Origin of Tektites. *Meteoritics and Planetary Sciences, 29*, 73-78.

O'Keefe, J. D., & Ahrens, T. J. (1982b). Cometary and Meteorite Swarm Impact on Planetary Surfaces. *Journal of Geophysical Research, 87*, 6668-6680.

Passey, Q. R., & Melosh, H. J. (1980). Effects of Atmospheric Breakup on Crater Field Formation. *Icarus, 42*, 211-233.

Petrovic, J. J. (2001). Review: Mechanical Properties of Meteorites and Their Constituents. *Journal of Materials Science, 36*, 1579-1583.

Stöffler, D. (1984). Glasses Formed by Hyper-Velocity Impact. *Journal of non-Crystalline Solids, 67* (1-3), 465-502.

Stöffler, D., & Langenhorst, F. (1994). Shock Metamorphism of Quartz in Nature and Experiment 1: Basic Observation and Theory. *Meteoritics and Planetary Science, 29* (2), 155-181.

Weibull, W. (1951). A Statistical Distribution Function of Wide Applicability. *Journal of Applied Mechanics, 18*, 140-147.

Chapter 2: An Investigation of the Whitecourt Meteorite Impact Crater (Alberta, Canada)

2.1 Introduction

Aside from experimental work, the investigation of the broad distribution of crater sizes in the terrestrial impact record has vastly improved understanding of these near instantaneous high-energy events. From metre-sized penetration craters to multi-kilometre hypervelocity impact basins, investigators may be faced with a number of site-specific challenges, the level of preservation often representing the most significant. In the smaller and generally younger structures, this may be the result of processes ranging from erosion to anthropogenic activity. Examples include the Morasko [e.g. Stankowski, 2001], Campo del Cielo [Cassidy, 1965], Carancas [Brown *et al.* 2008], Sikhote Alin [e.g. Krinov, 1966] and Haviland [Hodge, 1979] structures. In larger and generally older structures this may also involve subsequent burial, as in the case of Eagle Butte and Steen River [Robertson & Grieve, 1975], Obolon [e.g. Gurov *et al.* 2009] or Chesapeake Bay [Poag *et al.* 1992], or even tectonism as at the Sudbury impact structure [Dietz, 1964]. The result of low levels of preservation is that a single terrestrial crater rarely provides a complete record of the processes involved with its genesis. The Whitecourt Crater provides a rare exception in that it is well preserved, has an intact and easily observable ejecta blanket, and has associated meteorites. Table 2.1.1 provides a summary of known terrestrial impact structures of similar dimensions and age to the Whitecourt Crater.

The Whitecourt Impact Crater, located in central Alberta (Canada), represents a significant addition to the terrestrial impact record. The <1,100 year old crater, formed by the impact of a type IIIAB iron meteorite, is a simple bowl-shaped structure 36 m in diameter having a depth of 6 m as measured parallel to the local hill slope [Herd *et al.* 2008]. Its small size implies several possible formation scenarios, which vary in both impact velocity and impactor size. At the low-energy end of the impact spectrum a penetration crater forms as a result of low impact velocities, typically less than a few hundred metres per second [French, 1998]. The impactor, in this scenario, would be expected to survive relatively intact and remain buried within the immediate vicinity of the crater. The diameter of the resulting penetration crater is limited to a maximum of

several times the diameter of the impactor. At higher velocities explosively excavated craters result from high velocity or hypervelocity impact - generally at least 3 kilometres per second for most metals [e.g. Fair, 1987]. The impactor, in this scenario, is completely disrupted during impact. The fate of the impactor, whether it fragments, melts, vaporizes, or some combination of the three, is controlled primarily by impact velocity. These scenarios will be addressed qualitatively.

Table 2.1.1: Known craters having similar dimensions and ages to the Whitecourt Crater.[1]

Crater Name	Location	Diameter (km)	Age (ka)[2]	Target Material	Bolide Type[3]
Campo del Cielo	Argentina	0.05	< 4	Loess[4]	Coarse Octahedrite to Granular Hexahedrite
Carancas	Peru	0.0135	0.002	Unconsolidated Sediment[5]	H4-5 Chondrite[6]
Haviland	Kansas, U.S.A.	0.01	< 1	Unconsolidated Sediment[7]	Pallasite
Ilumetsä	Estonia	0.08	> 2	Sand/Siltstone[8]	-
Morasko	Poland	< 0.09	3.5-5[9]	Unconsolidated Sediment[9]	IAB Coarse Octahedrite[10]
Sikhote Alin	Russia	0.02	0.059	Loose Sediment[11]	Hexahedrite
Sobolev	Russia	0.05	< 1	Mixed[12]	Iron Meteoritic Material Found
Wabar	Saudi Arabia	< 0.116	0.14	Loose Sand[13]	IIIAB iron

[1] Obtained from the Earth Impact Database (2006) unless otherwise noted.
[2] Pre-1977 K-Ar, Ar-Ar and Rb-Sr ages recalculated using the decay constants of Steiger & Jager (1977).
[3] From Koeberl (1998) unless otherwise noted.
[4] [Cassidy *et al.* 1965]
[5] [Brown *et al.* 2008]
[6] [H. C. Connolly, Meteoritical Bulletin no. 93, Meteoritics & Planetary Science, 2008; Brown *et al.* 2008]
[7] [Hodge, 1979]
[8] [Raukas *et al.* 2001]
[9] [Stankowski, 2001 & 2007 and references therein]
[10] [Dominik, 1976]
[11] [Lang & Kowalski, 1973]
[12] Mixed implies sedimentary strata overlying crystalline rock
[13] [Shoemaker & Wynn, 1997]

In order to address the possible impact scenarios, we present field evidence collected during the course of field excursions to the site in 2008 and 2009. These data allow constraints on a number of parameters surrounding the Whitecourt impact event including the impact angle, impact velocity and fate of the impactor.

2.2 Regional Geology

The geological setting surrounding the Whitecourt Crater developed primarily in response to the erosion of the Rocky Mountains and subsequent glaciation and deglaciation associated with the advance and retreat of the Laurentide Ice Sheet. As a

result, Cretaceous to Tertiary sedimentary bedrock capped by Quaternary glacial deposits dominate the regional geology near the crater. The Paskapoo Formation, a highly heterogeneous fluvial mudstone and sandstone complex, comprises the local surface bedrock [Grasby *et al*. 2008; Tokarsky, 1977]. The overlying glacial deposits are part of the Prairie-Mackenzie (till) Province, of which over 80 % were derived from local bedrock and contain equivalent parts sand, silt and clay [Scott, 1976].

Outcrops located within several kilometres of the Whitecourt Crater provide insight into the association of the local bedrock and glacial till. These outcrops consist of a thin veneer of till sharply overlying a clean unconsolidated massive to bedded fine sand. Entrainment of the underlying unit in the till is restricted to within 10 to 30 cm of the contact. The thickness of the massive unconsolidated sand and the overlying till varies significantly. The sand reaches at least 3 m in thickness and the till, in one location, thickened by ~6 m over a horizontal distance of ~15 m. This sand unit sharply overlies either blocky mudstone or platy bedded sandstone which tends not to be laterally continuous. The sediments underlying the glacial till are likely part of the Lacombe Member of the Paskapoo Formation. The Lacombe Member is specifically characterized by siltstones, mudstones, channel and splay sandstones (very fine to medium grained), and minor coal beds. It may reach thicknesses of up to 300 m [Demchuk & Hills, 1991; Grasby *et al.* 2008].

The local soil profile is an orthic grey luvisol (Figure 2.2.1) [Soil Classification Working Group, 1998]. The profile begins at the surface with the modern soil composed of decomposing forest litter (O horizon) followed by a dark, organic-rich, silty very fine sand (Ah horizon). Beneath the Ah horizon, there is a sharp transition to pale silty very fine sand (Ae horizon). Below the Ae horizon there is a gradational increase in fines observed in pore-spaces and as grain coatings. At the Whitecourt Crater this transition zone (Bt horizon) is often thin and poorly defined. The parent material, at the base of the profile, is a pale grey to dark brown glacial till containing rare clasts up to ~15 cm in diameter (C horizon). The till is composed primarily of equal parts clay, silt and very fine sand. Granite and gneiss clasts comprise the dominant lithic fragments within the till with subordinate cm-scale mudstone and sandstone clasts.

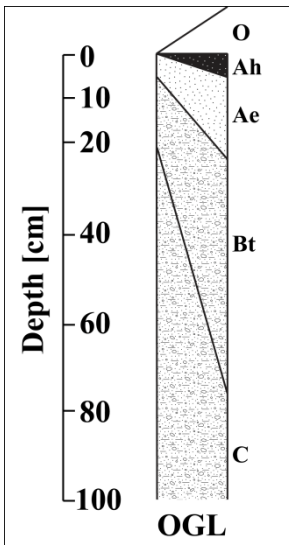

Figure 2.2.1: The Orthic Grey Luvisol (OGL) soil profile as observed in the area surrounding the Whitecourt Crater.

The Whitecourt Crater resides on a narrow northeastward sloping terrace immediately south of an ephemeral stream. The target sediments consist primarily of glacial till and, to a lesser extent, massive unconsolidated fine sand. The fine sand associated with the crater has only been observed within the ejecta, crater fill, and ~2.9 to 3.45 m beneath the crater floor and appears consistent with the fine sand observed at the outcrops discussed in the preceding paragraphs.

2.3 Methods

Work at the site focused on surface and subsurface investigations in addition to the search for meteorites. Surface elevation data and horizontal positioning were obtained primarily through the LiDAR data obtained from Airborne Imaging, Inc. (Calgary, Alberta). The locations of soil pits, boreholes and meteorites were recorded using handheld GPS units though, in most cases, these data were augmented by additional measurements. An Eijkelkamp hand auger, capable of reaching depths over 6 m, was used for subsurface sampling. The sampling chamber at the boring end of the auger is capable of providing a moderately undisturbed view of the sediments at ~10 to 15 cm intervals (Figure 2.3.1).

Subsurface information was collected primarily from soil pits for depths typically <0.5 m and boreholes for deeper observations. We have documented over 50 sample sites in addition to meteorite locations. Two cross-sections generated from these sample

sites delineate both the ejecta blanket, identified as the material overlying a local buried soil, or paleosol (Figure 2.3.1), and the crater fill distribution.

Figure 2.3.1: A sample of the paleosol and underlying Ah horizon used to delineate the ejecta blanket as revealed in the boring end of the auger. In this image the overlying ejecta represents ejected Ae horizon material. Charcoal is commonly associated with the paleosol. Way up is to the left.

Selected sediments obtained from varying depths and locations were analyzed either in bulk or as sieved samples. In particular, we were interested in finding evidence of impact generated melt or shock effects. Focus, therefore, was placed on samples collected from medial and distal ejecta in addition to sediments collected near the base of the transient crater boundary, where materials are expected to have experienced the greatest shock pressures. Magnetic grains collected from these samples were analyzed using a stereo microscope and, in select cases, a JEOL 6301F field emission scanning electron microscope (SEM). To search for non-magnetic melt and potentially shocked grains sediment samples were sieved either using a no. 200 (75 μm) or a no. 230 (63 μm) sieve and the residue analyzed initially using a stereo microscope. Quartz grains collected from the residue were subsequently viewed through an optical microscope using immersion oils (n = 1.572 and n = 1.550) and to search for planar fractures (PFs) or planar deformation features (PDFs) commonly associated with impacts [see Grieve *et al.* 1996 for a review]. Subsequent analyses of several planar microstructure (PM) bearing quartz grains were performed using the SEM. The filtrate of several proximal and distal ejecta samples were also analyzed quantitatively to search for evidence of atmospheric sorting.

Members of the research team, a number of Whitecourt area residents and several other volunteers were involved in the documented search for meteorites. The search was carried out primarily using metal detectors and, to a lesser extent, a magnetometer.

Where possible, meteorites were photographed *in situ* with markers indicating magnetic north. This was done for several samples having masses >300 g, collected during the latter part of the field campaign. Magnets were used to collect samples too small to easily identify or collect by hand. This was often the case for meteorites smaller than ~0.5 cm in longest dimension.

To investigate the possibility of a large buried being mass present at the site we conducted several magnetic and gradiometric surveys using GEM Systems' GSM 19-TW and the more sensitive 19-GW magnetometers. It was expected that such surveys would reveal magnetic anomalies that may be associated with the large buried mass required to form a penetration crater this size (possibly >10 m in diameter). Due to issues with the GPS sensor on the 19-GW, this instrument was used only to locate anomalies within the structure. A 100 m by 100 m grid centered on the crater was setup and walked using the 19-TW. The rover recorded measurements at 0.5 s intervals whereas the base station recorded measurements at 3.0 s intervals.

Chemical analyses of the meteorites at the crater are restricted primarily to the weathering products of several sub-cm fragments. These meteorite fragments were collected from the top of the contact between the diamict and massive unconsolidated fine sands ~2.9 m beneath the base of the crater. Two fragments were mounted in epoxy, sectioned, and polished. We've analyzed sections using a Cameca SX100 electron microprobe to generate X-ray elemental maps using Wavelength Dispersive Spectrometry (WDS). Material from the weathered rind of a third meteorite collected from this depth was crushed using a mortar and pestle and then magnetically separated using a technique similar to that of Chen *et al.* (2005). The resulting magnetic material was analyzed using a Rigaku Geigerflex Power Diffractometer (XRD). The remainder of the collected meteorites were cleaned using deionized water, acetone and soft brushes.

2.4 Results

2.4.1 The Impact Crater

The fact that the Whitecourt Crater has remained unidentified for so long attests to the obscuring nature of the local topography, vegetation and its relatively small size. The site is located within 40 m of two well-used ATV tracks, though is only partially visible from the north track during the winter months (Figure 2.4.1). Local topography

also introduces some variation in the actual crater dimensions, notably in crater depth. The rim elevation of the Whitecourt Crater varies by ~5 m resulting in an apparent depth range from ~5 m, as measured at the east rim, to ~10 m, as measured from the south rim. These measurements supplement the depth as measured parallel to the local slope as reported by Herd *et al.* (2008).

The overall structure of the Whitecourt Crater is similar to most simple bowl-shaped terrestrial craters with only a few exceptions. An overturned flap located near the crater rim, commonly associated with simple structures, has not been observed. It is also worth noting that the raised rim, which typically circumnavigates simple craters, only extends between the bearings ~020° and ~110°. The opposing side of the crater shows little evidence of uplift. Given the gentle nature of the target surface, it is unlikely that topography played a significant role in determining the crater rim morphology. This may be analogous to a depressed up-range rim and is discussed later. Surface contours within the crater are relatively circular and evenly spaced indicating that there has been no preferential crater wall steepening (Figure 2.4.1). The high elevation of the south rim is likely responsible for the distortion of the contours along that wall as tree trunks along the south wall show some evidence of creep.

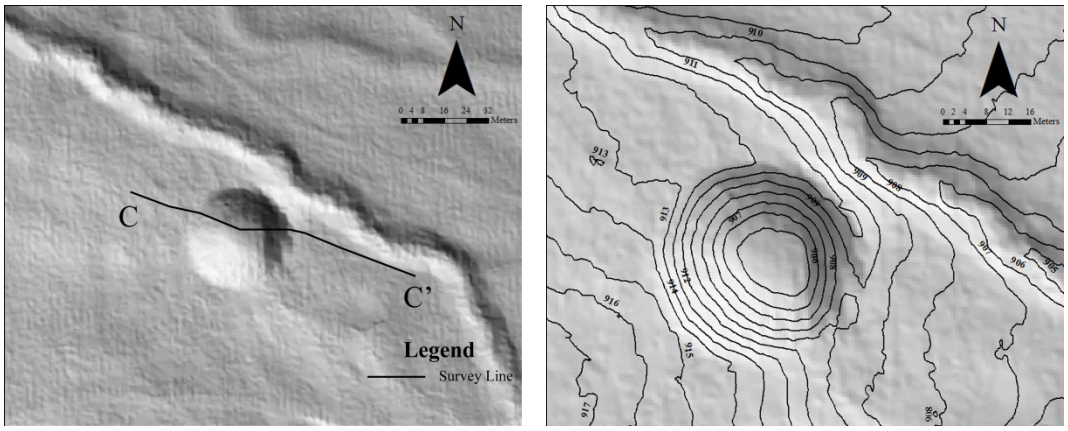

Figure 2.4.1: Left: LiDAR image of the crater and nearby surroundings. Right: Surface contours at 1 m intervals.

As discussed previously, glacial till and, to a lesser extent, fine sand dominate the target sediments. Within the immediate vicinity of the crater, we have been unable to determine the actual thickness of the till. At a site 18.5 m east of the crater rim the till reaches a thickness of at least 5.8 m, though this may not represent the thickness of the till at the point of impact (Figure 2.4.2). The local till has a uniform silty/clayey texture

and only appears to vary significantly in color. The well-sorted, unconsolidated massive fine sand present beneath the crater at depths below ~2.9 m to ~3.45 m is consistent with the fine sand observed in the crater fill and the small cm-scale sand lenses in the ejecta east and northeast of the crater. It extends to a depth of at least 5.41 m below the base of the crater floor; the local water table is not present above this depth. Sub-angular to angular quartz grains represent the bulk of the fine sand. No clear depositional structures were observed within this sand unit, though it is possible that any structures present at these depths have been disrupted by the impact and/or the process of boring. Figure 2.4.2 provides a general overview of the crater and target sediments.

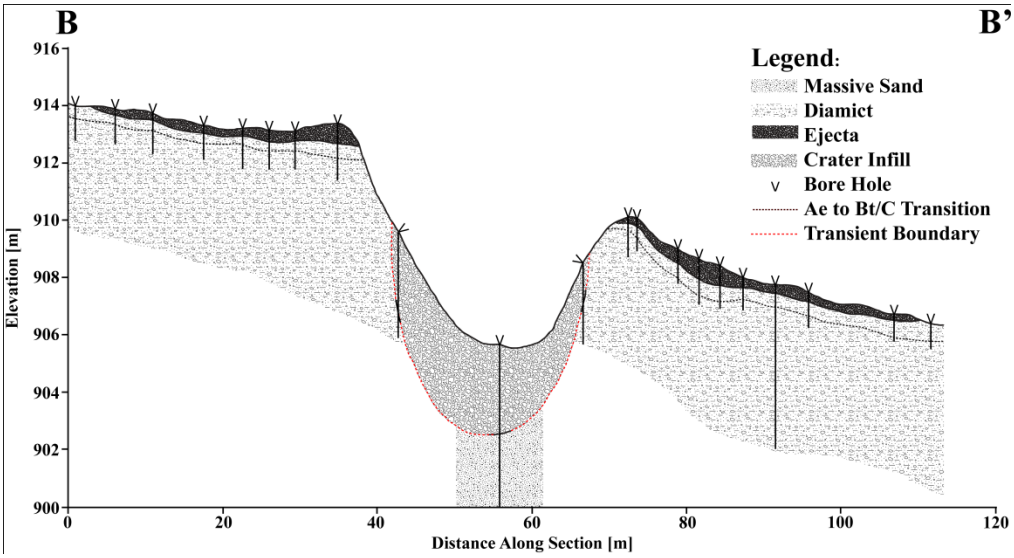

Figure 2.4.2: Summary cross-section through the crater along 110° (Figure 2.4.5). The transient crater boundary is constrained by five boreholes (the 4th and 5th are not included in this section). The base of the transient crater boundary is likely more irregular than displayed, due to the changes in sediment type. The center of the transient crater appears slightly offset towards the northeast. The depth to the transient crater boundary is ~2.9 m at the center of the crater floor [Herd *et al.* 2008] and ~3.45 m along the northeast crater floor – the surface is at the same elevation. The vertical exaggeration is 4.2.

The crater fill is largely a diamict, significantly more heterogeneous than the local till. Centimetre- to decimetre-scale sand lenses common in the crater fill are not observed in the local till. In addition, there is a coarse sand component present in much of the observed crater fill, likely derived from the underlying fine sand. Platy sandstone fragments, similar to those observed at several outcrops in the area, are also present within the crater fill. These fragments appear to be concentrated along the east crater wall and are up to 20 cm in longest dimension and typically ~1.5 cm thick. Contacts between the heterogeneous crater fill and the local till were found at depths of 1.35 m and

2.55 m along the east and west crater walls respectively (Figure 2.4.2). The underlying till at each contact is consistent with till located outside the area affected by the impact. We interpret the transition between the crater fill diamict and the massive unconsolidated sand at ~ 2.9 m and ~3.45 m to mark the depth to the transient crater boundary at the center and northeast corner of the crater floor, consistent with the interpretation of Herd *et al.* [2008] (Figure 2.4.2).

At present conclusive evidence of shock within the crater fill is limited. We have found no silicate melt and only rare samples of impactor melt within the crater fill, and below the transient crater boundary (Figure 2.4.3). Parallel planar microstructures in quartz grains are common within the fine sand beneath the transient crater boundary. However, almost all grains exhibiting parallel planar microstructures contain only one to three sets resolvable using optical microscopy, though this count can be difficult to ascertain for whole grains. Such grains have been recovered at depths up to 4.62 m beneath the center of the crater floor.

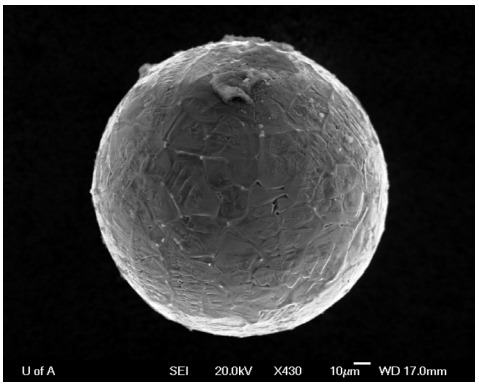

Figure 2.4.3: An SEM image of a 180 μm diameter Fe-Ni oxide spherule collected at the Whitecourt Crater. Recovery depth was 3.27 m beneath the northeast crater floor. (Norm wt%: Fe = 68.17, Ni = 8.20, Al = 0.41, O = 22.71).

2.4.2 The Ejecta Blanket

Mapping the distribution of the ejecta blanket and determining its approximate volume was one of the primary objectives of the investigation at the Whitecourt Crater. LiDAR imaging does not resolve the ejecta distribution. Additionally the LiDAR data reveal no surface features (grooves, ridges, ramparts or other forms providing evidence of radial flow) typically associated with non-terrestrial ejecta blankets. The ejecta distribution was determined by mapping the depth to the underlying paleosol (Figures

2.3.1 and 2.4.4), using boreholes and soil pits. This paleosol is continuous in the area adjacent to the crater. Figure 2.4.5 provides the locations of the soil pits and boreholes used to map the ejecta blanket. Using the depths and locations of the paleosol observed at the site, the original surface sloped ~9° to the east-northeast.

There is some variation in the organic content of the paleosol, a fragile dark organic-rich layer 3 to 5 cm thick commonly capped with a thin layer of charcoal, at the site. An Ah horizon, which may be up to 15 cm thick, typically underlies the paleosol. The preservation of the paleosol implies that the ejected sediments were deposited at velocities low enough to prevent incorporation of any underlying surface material. At locations where the paleosol lacked significant organic material, the depth was delineated by the contact between the base of the ejecta and the top of the underlying Ah horizon. Charcoal from the paleosol dated previously provides a maximum age for the crater of ~1.13 ka [Herd *et al.* 2008].

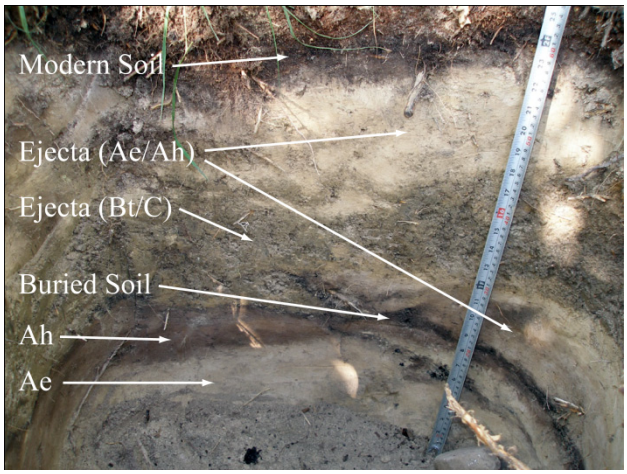

Figure 2.4.4: Proximal ejecta located at the first sample site southwest of the crater rim along the AA' (Figure 2.4.5). The horizons indicated represent the sediment from which the ejecta was derived.

The ejecta blanket distribution was determined using a series of boreholes along two lines transecting the crater. Several additional boreholes and soil pits confirmed that the ejecta blanket surrounds the crater. The thickness of the ejecta was measured along these transects and at various other sites as indicated in Figure 2.4.5. These thicknesses were also used to estimate ejecta blanket thickness at the regions not sampled so that the volume of the ejecta blanket could be determined. The resultant distribution reveals that the ejecta is concentrated to the east-northeast of the crater with limited bilateral symmetry. There does not appear to be a significant zone of avoidance, or forbidden

zone, characterized by a lack of ejecta, associated with the ejecta blanket [e.g. Shultz, 1992c]. Based on analysis using ArcGIS software, the ejecta covers an area of ~6000 m^2 having a volume of ~1,250 m^3 based on the distribution shown in Figure 2.4.5. For comparison, the volume of the crater is 2,900 m^3 [Herd *et al.* 2008].

The ejecta blanket is composed of three units. The two dominant units are diamict (derived from the Bt/C horizon) and the very fine sand (derived from the Ae/Ah horizon). The third unit is the fine sand, which is similar in appearance to the fine sand observed at depths >2.9 m beneath the crater floor. No large (decimetre-scale) fragments of sandstone have been observed within the ejecta blanket. The most proximal ejecta consist of diamict and very fine sand (Figure 2.4.4). The very fine sand and diamict are heavily disrupted and vary significantly in discrete unit size and distribution. The sharp contacts between these units suggest that subsequent modification due to soil forming processes is limited. There does not appear to have been significant mixing between the two units during excavation and deposition within at least 5 metres of the crater rim, consistent with the lower energies involved in proximal ejecta emplacement. The thickness of the most proximal ejecta varies between ~25 cm and ~80 cm.

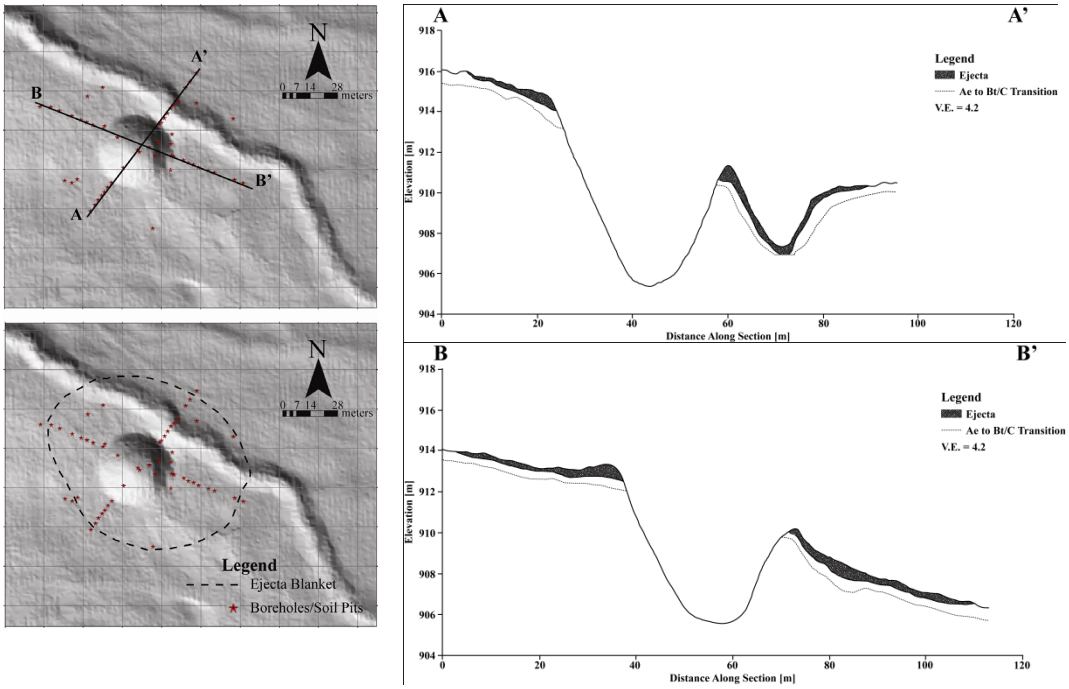

Figure 2.4.5: Cross-sections of the ejecta blanket along 038° and 110° with a reference figure showing the location of the sections. Approximate distribution of the ejecta blanket and the main soil pit and borehole site locations are also provided.

At roughly 1/3 extent along each transect only a single unit is observed at each site. Diamict comprises the dominant unit beyond this point, though the northern portion of the AA' transect has A horizon material at its terminus. The other three terminal points of each transect and other pits in more distal locations all have diamict as the ejected material. No deposition structures were observed within the ejecta (Figure 2.4.6).

Qualitative assessment of proximal and distal ejecta samples provides little evidence of sorting. Several samples filtered using a no. 200 (75 μm) sieve show only minor differences in fine content per volume sampled. In general, there appears to be a slightly higher proportion of silts and clays in the most distal material, though it remains a poorly sorted diamict. This difference could arguably relate to the heterogeneity in the diamict itself and not to any atmospheric sorting processes.

Figure 2.4.6: Images of the ejecta from proximal to distal (left to right). The center image includes an *in situ* meteorite located in the top right at the base of the modern soil.

No clear shock effects were observed in the ejecta. We found no melt products within the proximal, medial or distal ejecta. While magnetic grains are common within the till, with the exception of rare mm-scale meteorite fragments, the magnetic grains recovered from the ejecta appear to pre-date the impact and are present in till not affected by the event. Rare quartz grains containing single sets of parallel planar microstructures are present in medial and distal ejecta samples. Their rarity is likely due, in part, to the difficulty of working with the smaller quartz grain sizes present in the ejected sediments. The orientations of these planar microstructures have not been determined. It is worth noting parallel microstructures, while present, are extremely rare in quartz grains collected from the fine sand collected from other Paskapoo Formation outcrops; these

samples are not as planar as those observed in samples from the crater, and are likely the result of tectonism.

2.4.3 The Meteorites

The recovery of meteorites led to the discovery of the crater; known initially as an unusual depression to a number of local residents for over a decade. Little was thought of the depression until the two individuals that brought it to the attention of experts, James R. and Rodney Stevens, decided to search for meteorites at the site [Herd *et al.* 2008]. Since their initial discovery, over 1,200 meteorites have been collected with a cumulative mass approaching 50 kg.

The meteorites, with few exceptions, have similar jagged and angular morphologies (Figure 2.4.7A & 2.4.7B). Cut samples reveal the Widmanstätten pattern characteristic of Type IIIAB irons and include areas where the pattern was disrupted due to recrystallization [Herd *et al.* 2008], suggesting that their internal structure controls, in large part, their external morphology. In addition, the present suite of meteorites contains only a single 6.51 kg sample displaying evidence of well-defined atmospheric modification, including regmaglypts and a fusion crust (Figure 2.4.7C). The remaining samples lack a preserved fusion crust, atmospheric sculpting effects and regmaglypts. However, several of the Whitecourt meteorites arguably represent fragments initially situated at the surface of a larger body, which subsequently spalled off exposing a fresh unmodified surface with jagged edges.

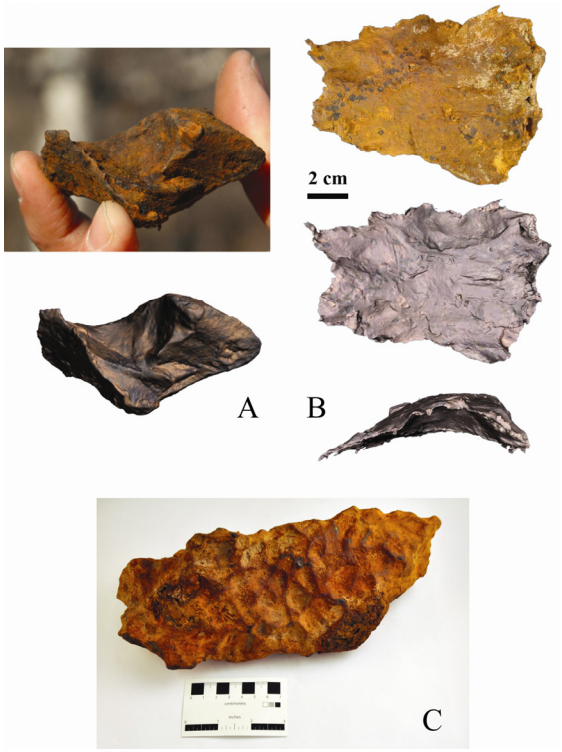

Figure 2.4.7: Images of two meteorites and their associated 3D scans. The masses of the samples are (A) 254 g and (B) 855 g. The photographs were provided by (A) Marie-Claude Williamson, Canadian Space Agency, and (B) Tiffany Borgel, University of Alberta. The 3D scans were generated by (A) R. Kofman and (B) Chris Want, University of Alberta, using a NextEngine desktop 3D laser scanner. The 6.51 kg meteorite (C) was found ~261 m east-northeast of the crater (Figure 2.4.8). This sample's surface is characterized by regmaglypts and an exposed fusion crust. Photograph by R. Kofman.

Figure 2.4.8 illustrates the known meteorite distribution. As of January 2010, most of the samples represent material collected by a volunteer search team outside the 200 m by 200 m area protected under the Alberta Provincial Historic Resources Designation Act [Herd *et al.*, 2008]; meteorite searching within the protected area is limited in order to preserve the crater and ejecta blanket. The distribution fans out along 065° to 075°, with most samples between 000° and 130°, and the crater located nearest the west-southwest boundary. The largest samples, those >200 g, range from within the crater to over 300 m beyond the crater rim. Fragments of meteoritic iron, having a mass <1 g, have been collected at both distal and proximal sites. At present, the most distal recovered sample is located over 350 m east-northeast of the crater. While the search for meteorites outside the protected area has focused on the northeast and southeast quadrants, searches were also conducted in the northwest and southwest quadrants with little success. The apparent concentration of smaller samples outside the protected area reflects, in part, the increased sensitivity of the detectors used by the volunteer team.

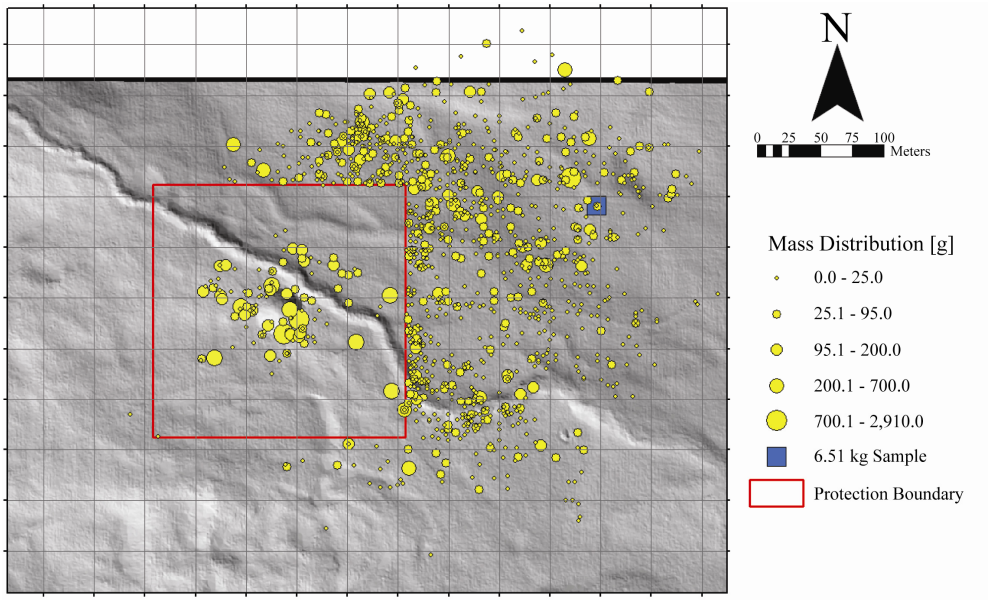

Figure 2.4.8: The mass distribution of meteorites at the time of writing. The distribution extends beyond the range of the LiDAR data. Many sites contain multiple samples. The grid spacing is 40 m.

The bulk of the meteorites have been collected at depths <25 cm, typically near the base of the modern soil. With few exceptions, meteorites found in association with the ejecta blanket lie at, or near, the upper contact with the modern soil (Figure 2.4.6 center); this may be due to the limited penetration depth of the metal detectors used to search near the crater. Where observed *in situ*, discoidal and dished meteorites typically lie flat with no evidence of preferred orientation (i.e. neither concave-up nor concave-down orientations appear favored). Meteorites found at greater depths within the ejecta are typically at depths <35 cm. These samples also show no preferred orientation. Meteorites collected beyond the range of the ejecta are typically located near base of the modern soil; the deepest (Figure 2.4.7C) recovered from a depth of ~40 cm.

Meteorites were also collected from various depths within the crater fill and immediately above the transient crater boundary. As these meteorites were collected in sample chamber of the auger head they are necessarily small, all <5 g. In addition to the small meteorites collected near the transient crater boundary dozens of micro- to millimetre scale meteoritic metal fragments were collected from sediment recovered above and below the transient crater boundary. This 'meteorite dust' [Krinov, 1966] is typically restricted to within 20 cm of the transient crater boundary with the bulk concentrated above, though some has been recovered from discrete lenses at shallower

depths within the crater fill. Two larger, unrecovered meteorites were found, one at the transient crater boundary and another within the crater fill at a depth of ~1.4 m along the south crater wall. These unrecovered meteorites have probable masses of several hundred grams.

A number of the small meteorites recovered at the transient crater boundary are analogous to the 'shale balls' observed at Meteor Crater [Barringer, 1909; Artemieva & Pierazzo, 2009]. The shale balls are, in this case, clasts of Fe-stained, Fe-oxide cemented target materials with meteoritic iron cores (Figure 2.4.9A). While it appears that there has been some weathering, particularly as evidenced by the diffusion of Ni from the fragment into the surrounding materials, it seems that the weathering process was relatively quick and/or short-lived, possibly halting once the weathered rind had formed. The brief weathering duration would explain the preservation of such fine textures and structures still preserved at the surface of the fragment (Figure 2.4.9B). These shale balls show more terrestrial alteration than the other meteorites. XRD analysis of these samples indicates that the dominant alteration products are goethite and magnetite/maghemite. The dense rind encapsulating the sample delineates the local limits of Fe and Ni diffusion as shown in Figure 2.4.9C. In contrast, the near surface meteorites, while showing signs of weathering, rarely have any local sediments cemented or otherwise fused to their surfaces. The resulting weathered rind on most near surface meteorites is typically several tens of micrometres to a millimetre thick, which in places has produced flaky textures. In rare cases, weathering has exposed the Widmanstätten grid.

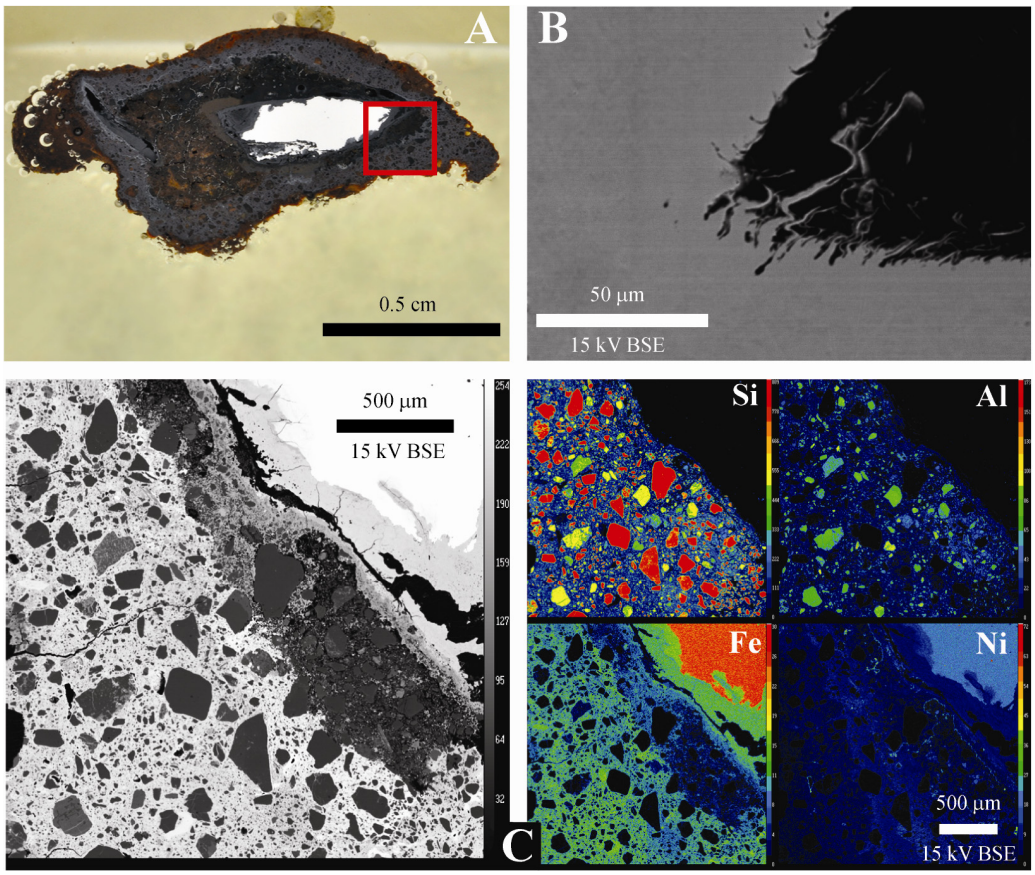

Figure 2.4.9: (A) A shale ball collected from the base of the transient crater. (B) A backscattered electron image of well-preserved filament-like surface texture on the metal core of one of the shale balls. The grey material in the image is meteoritic iron. (C) BSE image and elemental maps revealing the qualitative distribution of Si, Al, Fe and Ni for a portion of the shale ball delineated by the red square in (A).

Figure 2.4.10 illustrates data obtained from one of the magnetometer surveys. There are a number of positive and negative anomalies apparent in the figure (red and green respectively). Subsequent investigations of these anomalies have yielded several of the largest meteorites collected to date. At present, all of the anomalies found in the surveys appear related to near surface meteorites or magnets. With the meteorites removed, future surveys and forward modeling of the resulting data should provide a better view of the crater and immediate surroundings.

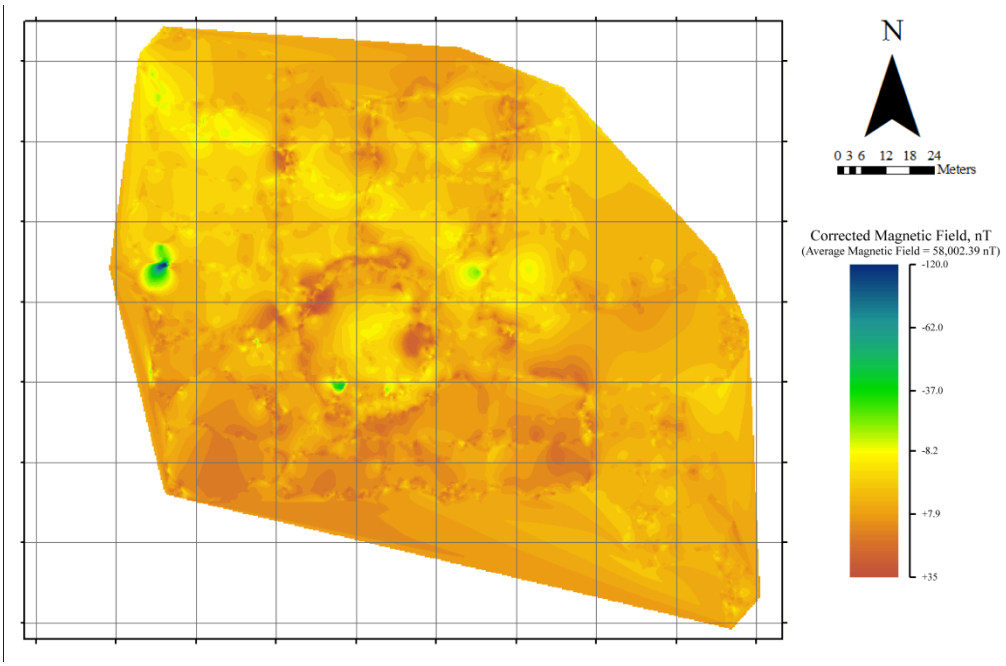

Figure 2.4.10: Combined results of two magnetic surveys performed using the GEM Systems GSM 19-TW. This represents the diurnally corrected data. Dense vegetation along the southern half of the grid made surveying slightly more difficult. A large magnet was found at the large positive anomaly on the NW crater rim (one of three found to date, likely left behind by meteorite hunters). With the exception of the magnet, large meteorites, about several hundred grams each, were found at all the major anomalies. Several other meteorites of similar scale were recovered from additional localized anomalies evident only in the raw data.

2.5 Discussion

In summary, the Whitecourt Crater is a circular bowl-shaped simple structure 36 m in diameter having a depth range of 5 m to 10 m. The crater floor is bowl-shaped, showing no evidence of having hosted standing water. The structure and underlying sediments, to a depth of at least 5.41 m, are located above the local water table. The crater walls do not show significant steepening along any orientation, though creep is apparent along southern wall. An impact-generated raised rim exists only along the northeast portion of the crater rim (Figure 2.4.1). The well-preserved ejecta blanket lacks a forbidden zone and is concentrated east-northeast of the crater. Shock effects observed within the ejecta blanket, crater fill and underlying sediments are limited to PM-bearing quartz grains, meteorite dust, and rare Fe-Ni oxide spherules, indicative of relatively low shock pressures and disruption and partial melting of the impactor. The associated meteorites, with one notable exception (Figure 2.4.7C), are typically jagged and show little evidence of high-velocity atmospheric transit alteration effects. They are concentrated near the base of the modern soil surrounding the crater; however, several

have been collected from greater depths within the ejecta and crater fill. Meteorite dust and several cm-scale meteorite fragments were also collected from the transient crater boundary.

At the Whitecourt Crater a combination of crater morphology, ejecta blanket and meteorite distributions constrain the flight path of the impactor. Regarding crater morphology, these features include the location and extent of the raised rim, the crater walls and overall shape. The circularity of the structure and lack of crater wall steepening along any specific bearing suggest an impact angle >~30° [Gault & Wedekind, 1978; Gault *et al.* 1965]. The raised rim, located on the northeast portion of the crater, is directly opposite a region showing no evidence of structural lift along the southwest (Figure 2.4.5, particularly along AA'). It is unlikely that post-impact modification has masked any significant structural uplift along the entire southwest half of the crater. Consequently, this may be analogous to the depressed up-range rim observed on much larger lunar and Venusian craters, which occur at impact angles between 40° and 45° [Herrick & Forsberg-Taylor, 2003]. The depressed and raised rim should form along the impactor's trajectory, which suggests that the incoming projectile was traveling along ~065° (Figure 2.5.1).

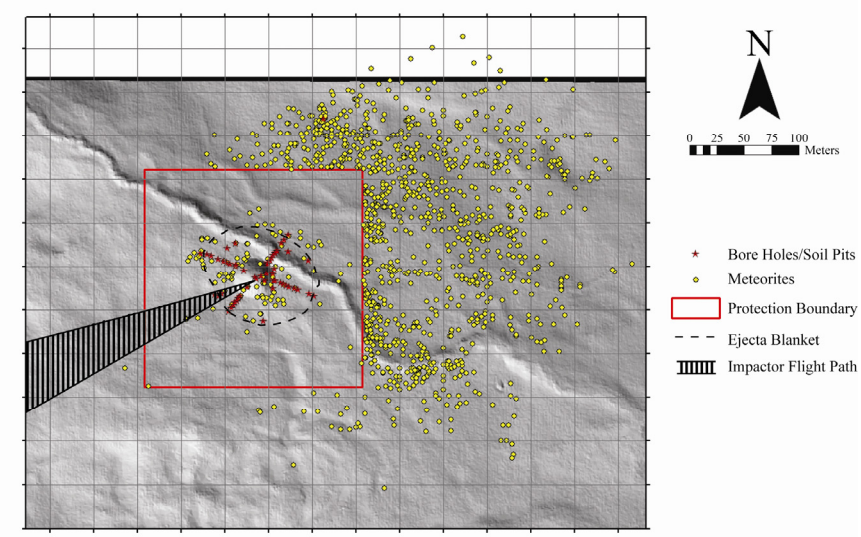

Figure 2.5.1: A summary diagram, which illustrates the meteorite distribution, local sample sites and boreholes, ejecta blanket and the proposed flight path of the impactor. Grid spacing is 40 m.

The distribution of the ejecta blanket provides another means of determining impactor trajectory. As shown in Figure 2.4.5 and 2.5.1, there is a clear concentration of ejecta towards the east-northeast with limited bilateral symmetry along that bearing. On

an airless body it has been determined that the ejecta distribution remains axially symmetric to an impact angle as low as ~45° with the concentration shifting down-range as the angle decreases, though the presence of an atmosphere increases the angle at which this occurs [Gault & Wedekind, 1978; Shultz 1992c; Melosh, 1989]. We have not observed a well-developed forbidden zone in the ejecta surrounding the Whitecourt Crater. It has been experimentally determined that a forbidden zone develops uprange at impact angles typically <45° in a vacuum [Gault & Wedekind, 1978; Shultz 1992c; Melosh, 1989]. This zone of avoidance develops at lower angles in the presence of an atmosphere [Herrick & Forsberg-Taylor, 2003; Schultz, 1992c]. For Venusian craters (again, much larger than the Whitecourt Crater) the ejecta blanket is concentrated downrange at angles <55°, slightly higher than would be expected on Earth [Herrick & Forsberg-Taylor, 2003]. Combining this with the crater morphology suggests that the Whitecourt impactor struck the surface at an angle likely between 40° to 55° while traveling towards ~060° to ~070°.

At terrestrial craters where meteorites are present, it is often possible to use their distribution to place constraints on the impactor's trajectory [e.g. Passey & Melosh, 1980]. In most cases, an incoming impactor will experience at least one major fragmentation event while traveling through the atmosphere resulting in its partial to complete disruption. The fragmentation process results in a large number of small fragments, which slow down and disperse, and a small number of large fragments, which maintain higher velocities and continue along a slightly modified trajectory. In an ideal situation for a significantly oblique trajectory, this will result in an elliptical strewnfield in which the meteorites would be relatively well sorted having the largest fragments (and associated craters under favorable circumstances) concentrated downrange and the smallest fragments concentrated up-range. The long axis of the resultant ellipse would represent the direction of flight of the original impactor. However, the distribution of the Whitecourt meteorites, being neither elliptical nor well sorted, does not appear to represent an ideal strewn field, though the distribution does appear to be controlled by the trajectory of the impactor. The direction of flight as constrained by the recovered meteorites, assuming that the fan-shaped distribution is bilaterally symmetric along the impact trajectory, is along 065° to 075°.

Observations of the Whitecourt Crater allow for several impact scenarios that involve the possible atmospheric fragmentation of the incoming meteoroid and the fate of the impactor during impact. The lack of a preserved fusion crust, regmaglypts, or other

atmospheric sculpting effects on the bulk of the meteorites suggest that they spent little or no time travelling through the atmosphere at the velocity required for ablation. We propose that they spalled off the main mass during impact. Additionally, the apparent depth to diameter ratio of the Whitecourt Crater (~1:6), similar to that of Meteor Crater, implies that the structure formed as a result of the impact of a single large mass, or near simultaneous impact of a tight swarm of meteorites [Artemieva & Pierazzo, 2009: Melosh & Collins, 2005]. However, this presupposes that the impact was hypervelocity and that the cratering mechanics are similar for the two structures. We conclude that any significant atmospheric fragmentation event must have occurred immediately prior to impact, and that there is a high probability that the impactor traversed the atmosphere without catastrophically fragmenting. High impactor strength, low velocities and shallow impact angles increase the probability of this occurrence [Shultz, 1992c]. The lone 6.51 kg sample in Figure 2.4.7C, which must have spalled off the main mass at some higher altitude, indicates that the incoming meteor was travelling at a velocity of at least several kilometers per second faster than the 3.0 km/s limit for ablation at sea level [Allen *et al.,* 1952; Passey & Melosh, 1980].

Two scenarios regarding the fate of the impactor are possible for a structure of this scale. In the first scenario, the main body of the impactor is preserved and remains buried in the immediate vicinity of the crater, as would be the case for a penetration crater. In the second scenario, the impactor is catastrophically disrupted during impact (fragmented, melted, and/or vaporized), as would be the case for an explosively excavated crater formed by a hypervelocity impact.

Evidence suggests that the incoming meteoroid was catastrophically disrupted during impact. Meteorite fragments spalling off the trailing edge of the impactor once it struck the surface seem the best explanation for the meteorite mass distribution. These spallation products would concentrate down-range and result in the 'shrapnel field,' or ‘spall field,’ observed at the site. The meteorite morphology also appears consistent with impact spallation and is analogous to the proximal meteorites recovered at Meteor Crater, though the Whitecourt samples are not as heavily shocked [e.g. Artemieva & Pierazzo, 2009]. In addition, the initial magnetic survey results do not reveal the presence of a large buried iron mass near, or below the crater. Further, the presence of small jagged shrapnel, meteorite dust and Fe-Ni oxide spherules at the base of the transient crater boundary and within the crater fill also strongly suggest impactor disruption and, therefore, that the crater was formed explosively.

Despite our efforts, the evidence of shock we have observed at the Whitecourt Crater is limited to the planar microstructures observed in quartz grains collected primarily from the fine sand beneath the crater floor and several Fe-Ni oxide spherules collected from within the crater fill. At present, the impact-origin of these planar features requires further confirmation. In particular, the determination of the orientations of the planar microstructures would provide crucial insights into their genesis. The lack of molten target material, rare impactor melt products and the presence of shrapnel-like meteorites having a well-preserved Widmanstätten pattern suggest that this impact occurred at a velocity lower than the 12 to 15 km/s velocities proposed for Meteor Crater [Artemieva & Pierazzo, 2009; Melosh & Collins, 2005]. The impact velocity is likely near the lower limit for an explosively excavated crater and is loosely constrained here as ranging from roughly 8 km/s to 10 km/s. Lower velocities are unlikely due to the rate of atmospheric deceleration from the initial cosmic velocity of the iron meteor along the proposed trajectory.

In summary, we propose that the Whitecourt Crater was formed by a relatively low-energy hypervelocity impact (from ~8 km/s to ~10 km/s) of an iron impactor traveling along a trend of 060° to 075°, striking the surface at an angle between 40° and 55°. The impactor appears to have transited the atmosphere essentially intact without experiencing catastrophic disruption except possibly immediately prior to striking the surface, resulting in a crater formed from the impact of a tightly bound swarm of meteoroids or single mass. The bulk of the meteorite distribution is therefore the result of spallation during impact.

Bibliography

Allen, W. A., Rinehart, J. S., & White, W. C. (1952). Phenomena Associated with the Flight of Ultra-Speed Pellets, Part I. Ballistics. *Journal of Applied Physics, 23*, 132-137.

Artemieva, N., & Pierazzo, E. (2009). The Canyon Diablo Impact Event: Projectile Motion Through the Atmosphere. *Meteoritics & Planetary Science, 44* (1), 25-42.

Artemieva, N., & Shuvalov, V. (1996). Interaction of Shock Waves During the Passage of a Disrupted Meteoroid Through the Atmosphere. *Shock Waves, 5*, 359-367.

Artemieva, N., & Shuvalov, V. (2001). Motion of a Fragmented Meteoroid Through the Planetary Atmosphere. *Journal of Geophysical Research, 106*, 3297-3309.

Barringer, D. M. (1909). *Meteor Crater (Formerly called Coon Mountain or Coon Butte), in Northern Central Arizona.* Read before National Academy of Sciences: Princeton University. Privately Printed.

Brown, P., ReVelle, D. O., Silber, E. A., Edwards, W. N., Arrowsmith, S., Jackson, L. E., et al. (2008). Analysis of a Crater-Forming Impact in Peru. *Journal of Geophysical Research, 113*.

Cassidy, W. A., Villar, L. M., Bunch, T. E., Kohman, T. P., & Milton, D. J. (1965). Meteorites and Craters of Campo del Cielo, Argentina. *Science, New Series, 149* (3688), 1055-1064.

Chao, E. C., Fahey, J. J., Littler, J., & Milton, D. J. (1962). Stishovite, SiO_2, a very High Pressure new Mineral from Meteor Crater, Arizona. *Journal of Geophysical Research, 67*, 419-421.

Chao, E. C., Shoemaker, E. M., & Madsen, B. M. (1960). First Natural Occurence of Coesite. *Science , 132*, 220-222.

Chen, T., Xu, H., Xie, Q., Chen, J., Ji, J., & Lu, H. (2005). Characteristics and Genesis of Maghemiite in Chinese Loess and Paleosols: Mechanism for Magnetic Susceptibility Enhancement in Paleosols. *Earth and Planetary Science Letters, 240*, 790-802.

Chyba, C. F., Thomas, P. J., & Zahnle, K. J. (1993). The 1908 Tunguska explosion: Atmospheric disruption of a stony asteroid. *Nature, 361*, 40-44.

Database, E. I. (2006). Retrieved July 2008, from <http://www.unb.ca/passc/ImpactDatabase/>

Demchuk, T. D., & Hills, L. V. (1991). A Re-examination of the Paskapoo Formation in the Central Alberta Plains: The Designation of Three New Members. *Bulletin of Canadian Petroleum Geology, 39*, 270-282.

Dietz, R. S. (1964). Sudbury Structure as an Astrobleme. *The Journal of Geology, 72* (4), 412.

Dominik, B. (1976). Mineralogical and Chemical Study of Coarse Octahedrite Morasko (Poland). *Prace Mineralogiczne, no. 47*, 61 p.

Fair, H. (1987). Hypervelocity Then and Now. *Int. J. Impact Engng , 5*, 1-11.

Foschini, L. (2001). On the Atmospheric Fragmentation of Small Asteroids. *Astronomy & Astrophysics, 365*, 612-621.

French, B. M. (2004). The Importance of Being Cratered: The New Role of Meteorite Impact as a Normal Geological Process. *Meteorics & Planetary Science, 39* (2), 169-197.

French, B. M. (1998). *Traces of Catastophe: A Handbook of Shock-Metamorphic Effects in Terrestrial Meteorite Impact Structures.* LPI Contribution No. 954, Lunar and Planetary Institute, Houston. 120 pp.

Gault, D. E., & Wedekind, J. A. (1978). Experimental Studies of Oblique Impact. *Proc. Lunar Planet. Sci. Conf. 9th*, 3843-3875.

Gault, D. E., Quaide, W. L., & Oberbeck, V. R. (1965). Interpreting Ranger Photographs from Impact Cratering Studies. In W. N. Hess, D. H. Menzel, & J. A. O'Keefe, *The Nature of the Lunar Surface* (pp. 125-140). Baltimore: The Johns Hopkins Press.

Grasby, S. E., Chen, Z., Hamblin, A. P., Wozniak, P. R., & Sweet, A. (2008). Regional Characterization of the Paskapoo Bedrock Aquifer System, Southern Alberta. *Canadian Journal of Earth Sciences, 45*, 1501-1516.

Grieve, R. A., Langenhorst, F., & Stöffler, D. (1996). Shock Metamorphism of Quartz in Nature and Experiment: II. Significance in Geoscience. *Meteoritics & Planetary Science, 31*, 6-35.

Group, S. C. (1998). *The Canadian System of Soil Classification* (3rd ed., Vols. Agric. and Agri-Food Can. Publ. 1646 (Revised)). Ottawa: National Research Council of Canada.

Gurov, E., Gurova, E., Chernenko, Y., & Yamnichenko, A. (2009). The Obolon Impact Structure, Ukraine, and its Ejecta Deposits. *Meteoritics & Planetary Science, 44* (3), 389-404.

Herd, C. D., Froese, D. G., Walton, E. L., Kofman, R. S., Herd, E. P., & Duke, M. J. (2008). Anatomy of a Young Impact Event in Central Alberta: Prospects for the 'Missing' Holocene Impact Record. *Geology , 36* (12), 955-958.

Herrick, R. R., & Forsberg-Taylor, N. K. (2003). The Shape and Appearance of Craters Formed by Oblique Impact on the Moon and Venus. *Meteoritics & Planetary Science, 38* (11), 1551-1578.

Hodge, P. W. (1979). Meteoritic Material in the Soil Near Two Meteorite Craters (Abstract). *Meteoritics, 14*, 422-423.

Hodge, P. W. (1979). The Location of the Haviland Meteorite Crater. *Meteoritics & Planetary Sciences, 14* (2), 233-234.

Kenkmann, T., Artemieva, N. A., Wünnemann, K., Poelchau, M. H., Elbeshausen, D., & Núñez del Prado, H. (2009). The Carancas Meteorite Impact Crater, Peru: Geologic Surveying and Modeling of Crater Formation and Atmospheric Passage. *Meteoritics & Planetary Science, 44* (7), 985-1000.

Kieffer, S. W. (1971). Shock Metamorphism of the Coconino Sandstone at Meteor Crater, Arizona. *Journal of Geophysical Research, 76*, 5449-5473.

Kieffer, S. W., Phakey, P. P., & Christie, J. M. (1976). Shock Processes in Porous Quartzite: Transmission Electron Microscope Observations and Theory. *Contributions to Mineralogy and Petrology, 59*, 41-93.

Koeberl, C. (1986). Geochemistry of Tektites and Impact Glasses. *Annual Review of Earth and Planetary Sciences, 14*, 323-350.

Koeberl, C. (1998). Identification of meteoritic components in impactites. *Geological Society Special Publications, 140*, 133-153.

Koeberl, C. (1994a). Tektite Origin by Hypervelocity Asteroidal or Cometary Impact: Target Rocks, Source Craers, and Mechanisms. In B. O. Dressler, A. F. Grieve, & V. L. Sharpton (Eds.), *Large Meteorite Impacts and Planetary Evolution* (pp. 133-151). Geological Society of America Special Paper 293.

Krinov, E. L. (1966). *Giant Meteorites* (1st english ed.). New York: Pergamon Press.

Lang, B., & Kowalski, M. (1973). Sikhote Alin Meteoroid: A Contribution to the Story of its Fragmentation and Fragment Scattering. *Earth and Planetary Science Letters*, 85-90.

Melosh, H. J. (1989). *Impact Cratering : A Geologic Process.* New York: Oxford University Press.

Melosh, H. J., & Collins, G. S. (2005). Meteor Crater formed by low-velocity impact: The paucity of melted rock in this crater may be due to the striking projectile's speed. *Nature, 434*, 157.

Mittlefehldt, D. W., See, T. H., & Hörz, F. (1992). Dissemination and Fractionation of Projectile Materials in the Impact Melts from Wabar Crater, Saudi Arabia. *Meteoritics and Planetary Science, 27*, 361-370.

O'Keefe, J. A. (1994). Origin of Tektites. *Meteoritics and Planetary Sciences, 29*, 73-78.

O'Keefe, J. D., & Ahrens, T. J. (1982b). Cometary and Meteorite Swarm Impact on Planetary Surfaces. *Journal of Geophysical Research, 87*, 6668-6680.

Passey, Q. R., & Melosh, H. J. (1980). Effects of Atmospheric Breakup on Crater Field Formation. *Icarus, 42*, 211-233.

Poag, C. W., Powars, D. S., Poppe, L. J., Mixon, R. B., Edwards, L. E., Folger, D. W., et al. (1992). Deep Sea Drilling Project Site 612 Bolide Event: New Evidence of a Late Eocene Impact-Wave Deposit and a Possible Impace Site, U.S. East Coast. *Geology, 20* (9), 771-774.

Raukas, A., Tiirmaa, R., Kaup, E., & Kimmel, K. (2001). The Age of the Ilumetsa Meteorite Craters in Southeast Estonia. *Meteoritics & Planetary Science, 36*, 1507-1514.

Roberston, P. B., & Grieve, R. A. (1975). Impact Structures in Canada: Their Recognition and Characteristics. *The Journal of the Royal Astronomical Society of Canada, 69* (1), 1-21.

Schultz, P. H. (1992b). Atmospheric Effects on Ejecta Emplacement. *Journal of Geophysical Research, 97* (E7), 11,623-11,662.

Schultz, P. H. (1992c). Atmospheric Effects on Ejecta Emplacement and Crater Formation on Venus from Magellan. *Journal of Geophysical Research, 97* (E10), 16183-16248.

Scott, J. S. (1976). Geology of Canadian Tills. In R. F. Legget (Ed.), *Glacial Till* (Vol. 12, pp. 50-66). Ottawa: Royal Society of Canada.

Shoemaker, E. M., & Wynn, J. C. (1997). Geology of the Wabar Meteorite Craters, Saudi Arabia (Abstract). *Lunar and Planetary Science XXVIII*, 1313-1314.

Stankowski, W. T. (2001). The Geology and Morphology of the Natural Reserve "Meteoryt Morasko". *Planetary and Space Science, 49*, 749-753.

Stankowski, W. T., Raukas, A., Bluszcz, A., & Fedorowicz, S. (2007). Luminescence Dating of the Morasko (Poland), Kaali, Ilumetsa and Tsoorikmae (Estonia) Meteorite Craters. *Geochronometria, 28*, 25-29.

Steiger, R. H., & Jager, E. (1977). Subcommission on geochronology: convention of the use of decay constants in geo- and cosmochronology. *Earth Planet. Sci. Lett., 36*, 359-362.

Stöffler, D. (1984). Glasses Formed by Hyper-Velocity Impact. *Journal of non-Crystalline Solids, 67* (1-3), 465-502.

Stöffler, D., & Langenhorst, F. (1994). Shock Metamorphism of Quartz in Nature and Experiment 1: Basic Observation and Theory. *Meteoritics and Planetary Science, 29* (2), 155-181.

Tokarsky, O. (1977). The Hydrogeological Reconnaissance Maps of Alberta: Map 114. *Alberta Research Council Bulletin 35 - Contributions to the Hydrogeology of Alberta* . (J. Toth, Ed.) Alberta Research Council Groundwater Division.

Trenhaile, A. S. (2004). *Geomorphology A Canadian Perspective* (2nd ed.). New York: Oxford University Press.

Weibull, W. (1951). A Statistical Distribution Function of Wide Applicability. *Journal of Applied Mechanics, 18*, 140-147.

Chapter 3: Concluding Remarks

The results of this investigation of the Whitecourt Crater provide the initial observations and interpretations of the events surrounding this exceptional site. Table 3.1 provides an overview of the results of both the observations and modeling of the Whitecourt impact event. I expect that future work, particularly with respect to impact modeling, will improve upon the result below. My hope is that this work, in the very least, will provide a stepping-stone for future studies of the site and will provide valuable data to be used for the improvement of current impact models and the development of future models.

Table 3.1: A summary of the core results of the investigation of the Whitecourt Crater.

Atmospheric Entry Parameters:	
Radius*	0.35 m to 0.40 m
Velocity*	12 km/s to 16 km/s
Entry Angle*	41° to 56° to Surface of Earth
Impact Parameters:	
Radius*	0.25 m to 0.33 m
Velocity	8 km/s to 10 km/s
Impact Angle	40° to 55° to the Surface of Earth
Direction of Flight	Along 060° to 075°
Crater Parameters:	
Final Crater Diameter	36 m
Final Crater Depth [m]** [1]	6 m
Transient Crater Diameter [m]	~29 m
Max. Transient Crater Depth [m]***	~10.5 m
Meteorite Parameters:	
Meteorite Type [2]	IIIAB Iron, Medium Octahedrite
Samples Collected	>1,200
Mass Collected	~50 kg

* Based on modeling
** As measured parallel to the local hill slope
*** Considering the depth of the transient crater boundary below the 6 m crater depth
[1, 2] Herd *et al.* (2008)

I would like to conclude by mentioning several items not addressed to my satisfaction in this study. Of particular interest are the constraints placed on the transient crater boundary, the excavation depth, the orientations of the PMs observed in recovered quartz grains, and the meteorite distribution. The apparent offset, towards the northeast, of the base of the transient crater requires further study. I feel it important to determine if

this observation is consistent; at present it is based on a single borehole. The depth and orientation of the transient cavity is also related to the excavation depth and the depth of the contact between the till and the underlying Paskapoo Formation. Determining the depth of the contact near the crater rim should provide some indication whether the transient crater offset, if it is truly offset, is related to the momentum of the impactor, or is related to changes in sediment type. Additionally, the transient crater has been constrained only along its base and east/west boundaries. Several attempts were made to locate the transient crater boundaries along the north and south walls. However, obstructions within the crater fill prevented the boreholes from reaching depths >~2 m, above which a contact between the crater fill and parautochthonous sediments were not observed.

The orientations of the PMs in the recovered quartz grains would provide crucial insight regarding their origin. If the orientations prove to be consistent with those expected for PDFs, they could provide a means of determining the distribution of shock pressures beneath the crater and provide natural examples of relatively weakly shocked quartz. If they prove not to be consistent with PDFs, we are left to determine the processes responsible for their origin.

The search for meteorites outside the protected area has been thorough; though significantly more time has been spent searching where the concentration is greatest. The meteorite distribution outside the protected area, therefore, provides a good representation of the actual distribution. Certainly more searching could be done south and west of the crater in addition to using tools having greater depth penetration, though discoveries will likely occur at an exceedingly slow rate. The protected area requires further investigation. While a great deal of searching has been conducted near the crater, typically with lower quality detectors, the regions approaching the protection boundary have been largely neglected. Thorough investigation of the region immediately inside the protection boundary should provide further evidence as to the accuracy of the distribution outside the boundary. I would expect the distributions within and without the boundary to line up along the proposed trajectory of the impactor.

Bibliography

Herd, C. D., Froese, D. G., Walton, E. L., Kofman, R. S., Herd, E. P., & Duke, M. J. (2008). Anatomy of a Young Impact Event in Central Alberta: Prospects for the 'Missing' Holocene Impact Record. *Geology, 36* (12), 955-958.

Appendix:

Appendix 1 – Compositional Analysis of Whitecourt Sediments:

XRD analysis of several samples was used to determine if the sediments found at the outcrops are similar to those at the crater (i.e. to determine if the sands and sandstones observed at the crater are part of the Paskapoo Formation). For the sandstone samples, 0.5 cm cubes cut from the center of the thickest portion of each sample were crushed and analyzed to limit near surface contamination. The results of the analysis are included below in Figure A.1.1. Figure A.1.2 provides the locations of the outcrops. While this data is not conclusive, the bulk sands are very similar in composition. Additionally, the sandstone samples, which appear nearly identical as hand specimens, differ primarily due the additional calcite present in the Road Cut 01 sample.

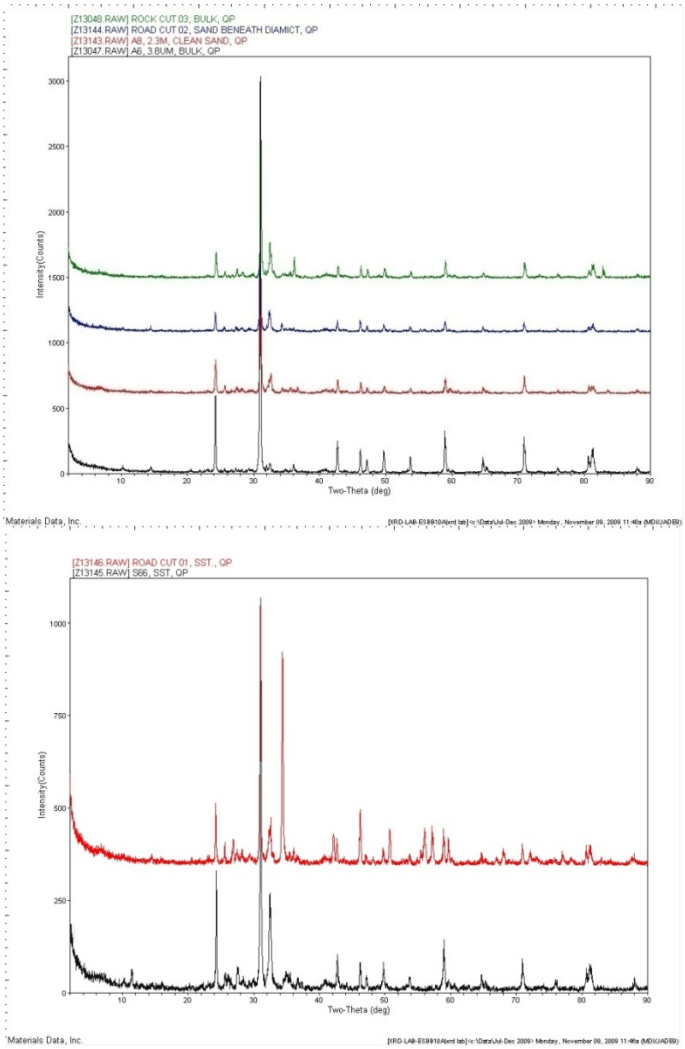

Figure A.1.1: The results of the XRD analysis of the bulk massive unconsolidated fine sand (top) and bulk sandstone samples (bottom) collected from the crater and several outcrops near the crater. Analysis performed by Diane Caird, from the University of Alberta.

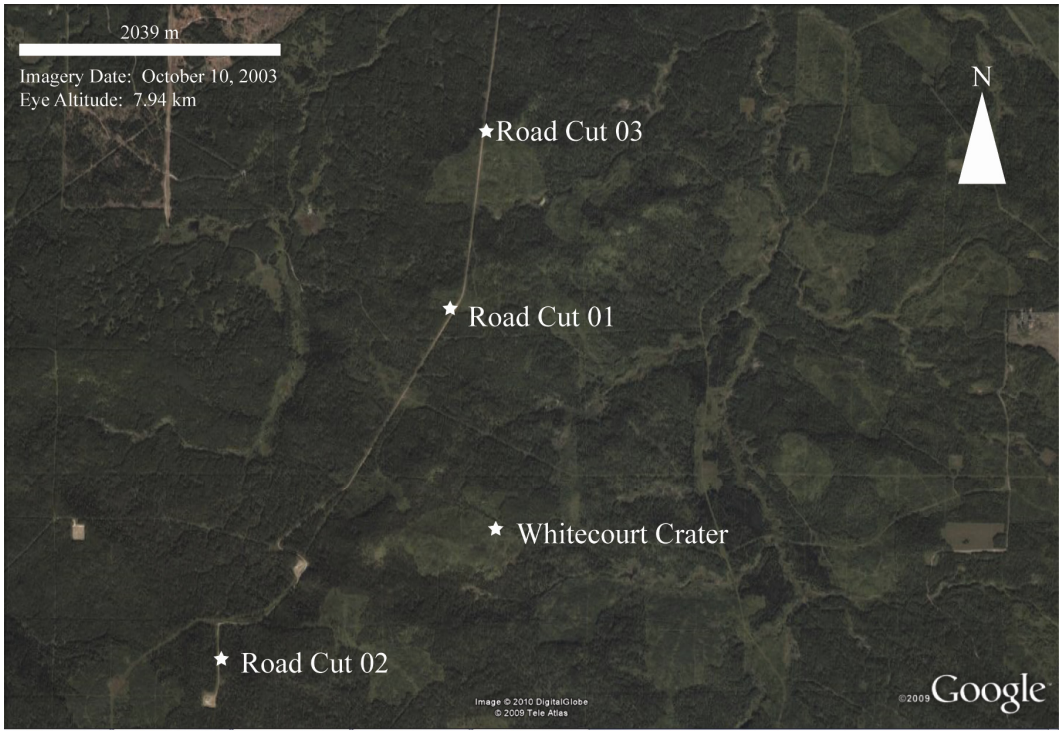

Figure A.1.2: The location of the main outcrops used in the study. GPS coordinates: Road Cut 01 = 1.8 km north of crater (Region 11U: 591568 5986030 - NAD83), Road Cut 02 = 2.3 km west-southwest of crater (Region 11U: 589818 5983309 - NAD83), Road Cut 03 = 3.0 km north of the crater (Region 11U: 591770 5987424 - NAD83).

Appendix 2 – Shock Effects:

Objective

The objective of this project was to identify potential shock effects hosted in sediments collected at the Whitecourt Crater.

Theory

Chapter 1 of this thesis provides a general overview of this subject, in addition to a number of references to pertinent review papers. One addendum involves the expected locations of shocked material. Shocked material and melt should be concentrated near the transient crater boundary, particularly along the crater floor, and in the distal ejecta [e.g. French, 1998; Melosh, 1989].

Methods

As noted previously the most highly shocked material should be concentrated at the base of the crater near the transient crater boundary and in the distal ejecta; this is where I focused my investigation. Evidence of melt and vaporization were sought primarily in the crater fill immediately above the transient crater boundary and within the distal ejecta. The shocked quartz grains, however, were sought from the proximal, medial and distal ejecta, in addition to the sand below the transient crater boundary to a maximum depth of 4.62 m. The transient crater boundary, defined as the transition between crater fill diamict and the *in situ* target sediments (massive sand or till), was at a depth of ~2.9 m at this location.

Sediment samples collected from the various sites were first analyzed using a stereo microscope. Where necessary, the dry clumpy clay-rich samples were gently broken down using a mortar and pestle. Most samples were then filtered using a no. 200 (75 μm) or no. 230 (63 μm) sieve to remove the silts and clays. Magnetic material was then collected from each sample using a rare earth magnet. The residue and magnetic grains were subsequently investigated under the stereo microscope for any evidence of melting (spherules, microtektites, etc.). Clasts of interest were then analyzed with the assistance of George Braybrook and De-Ann Rollings, from the University of Alberta,

using a JEOL 6301F field emission scanning electron microscope (SEM). Analyses included both exterior and interior surfaces, where possible.

The search for shocked quartz grains followed a more evolutionary path, which will not be described here, leading to the following technique. A small sample of the above residue was cleaned sonically and then dried. Small quantities of the clean sediments were then mounted in Cedar wood oil having a refractive index, n, of ~1.52 and viewed using an optical microscope. The mounted grains were rolled around using forceps, or dental picks, so that they could be viewed at various orientations in the hope of spotting grains bearing parallel planar microstructures (PMs). Suspect grains were removed and stored separately. Photomicrographs of many suspect grains were taken while they were in an immersion oil having n = 1.572 or n = 1.550 depending on what was currently available. Grain composition (SiO_2) was determined using the SEM.

Upon suggestion of Christian Koeberl, from the University of Vienna, the effects of hydrofluoric acid (HF) etching were investigated. Two different techniques were attempted, based on Gratz *et al.* (1996). The first technique attempted was HF vapor etching. This was performed on a polished mount of a small unsorted sample of cleaned fine sand from beneath the transient crater boundary. A small quantity of 49 % HF solution (~10 mL) was placed in a small HF acid resistant beaker and the polished mount placed faced down across the top of the beaker. The sample was left there for three minutes, removed, soaked in sodium bicarbonate to neutralize the HF and then rinsed with de-ionized water. This was done twice for the sample.

Liquid etching the individual quartz grains required more work. Small amounts of PM-containing grains were first placed in folded filter paper. Separate groups of grains were then submerged in the 49 % HF solution for periods of 0.5 minutes, 1.5 minutes and 3 minutes. The packet of grains was then placed in a saturated sodium bicarbonate solution and gently agitated until all evidence of reaction ceased (typically 5 to 6 minutes). The packet was then rinsed with de-ionized water, unfolded and relieved of the quartz grains. Unfortunately, the recovery rate was typically ~50 %. It is unclear if the grains were dissolved and lost in the filter paper or 'bubbled away' during the neutralization process. Figure A.2.1 illustrates another possible etching procedure. Many of the etched grains were subsequently analyzed using the SEM. As a side note, immersion oils interfered with SEM analysis; toluene can be used to remove immersion oil coating the grains; ethyl alcohol can then be used to remove the residual toluene.

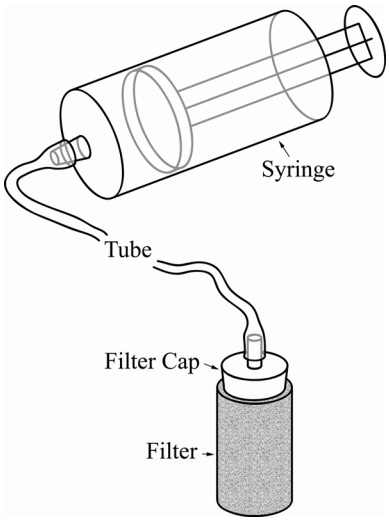

Procedure:

- Place the grains in the filter
- Attach the filter cap and sodium bicarbonate solution-filled syringe
- Place filter in 30 % HF acid until grains are completely submerged and gently agitate
- At the appropriate time remove filter from HF acid and suspend it in an empty HF acid resistant beaker
- Gently flush the sodium bicarbonate solution through the filter to neutralize the HF acid
- Remove the filter cap, rinse with deionized water and collect the samples

Figure A.2.1: A possible apparatus and procedure for etching grains in HF. The neutralizing reaction is quite vigorous.

Observations and Discussion

The observations are presented in Figures A.2.2 to A.2.4.

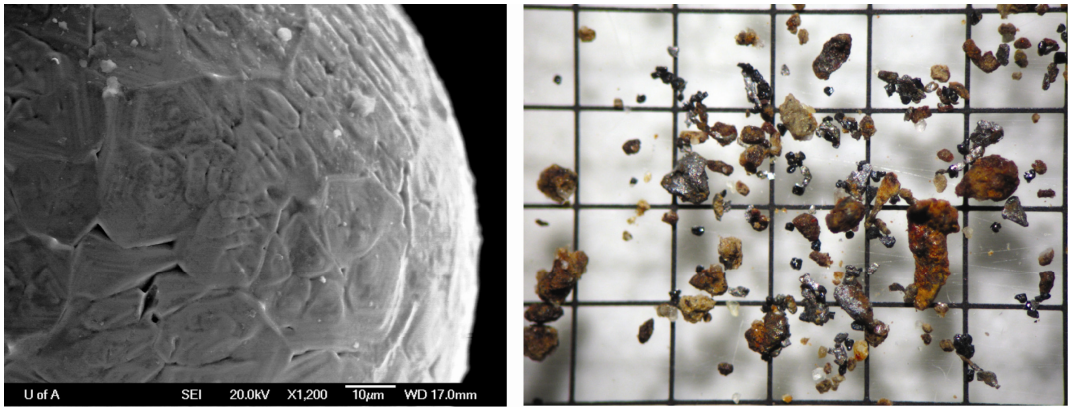

Figure A.2.2: Several impact shock products representing (left) shock melting of the impactor, a 180 μm diameter Fe-Ni oxide spherule(Figure 2.4.3); and (right) fragmentation of the impactor, 'meteorite dust.' The image on the right contains meteoritic metal, both clean and weathered fragments, in addition to some non-meteoritic magnetic and non-magnetic fragments. This particular sample of meteorite dust was collected at the transient crater boundary located under the center of the crater at a depth of ~2.9 m. The grid spacing on the right is 1 mm.

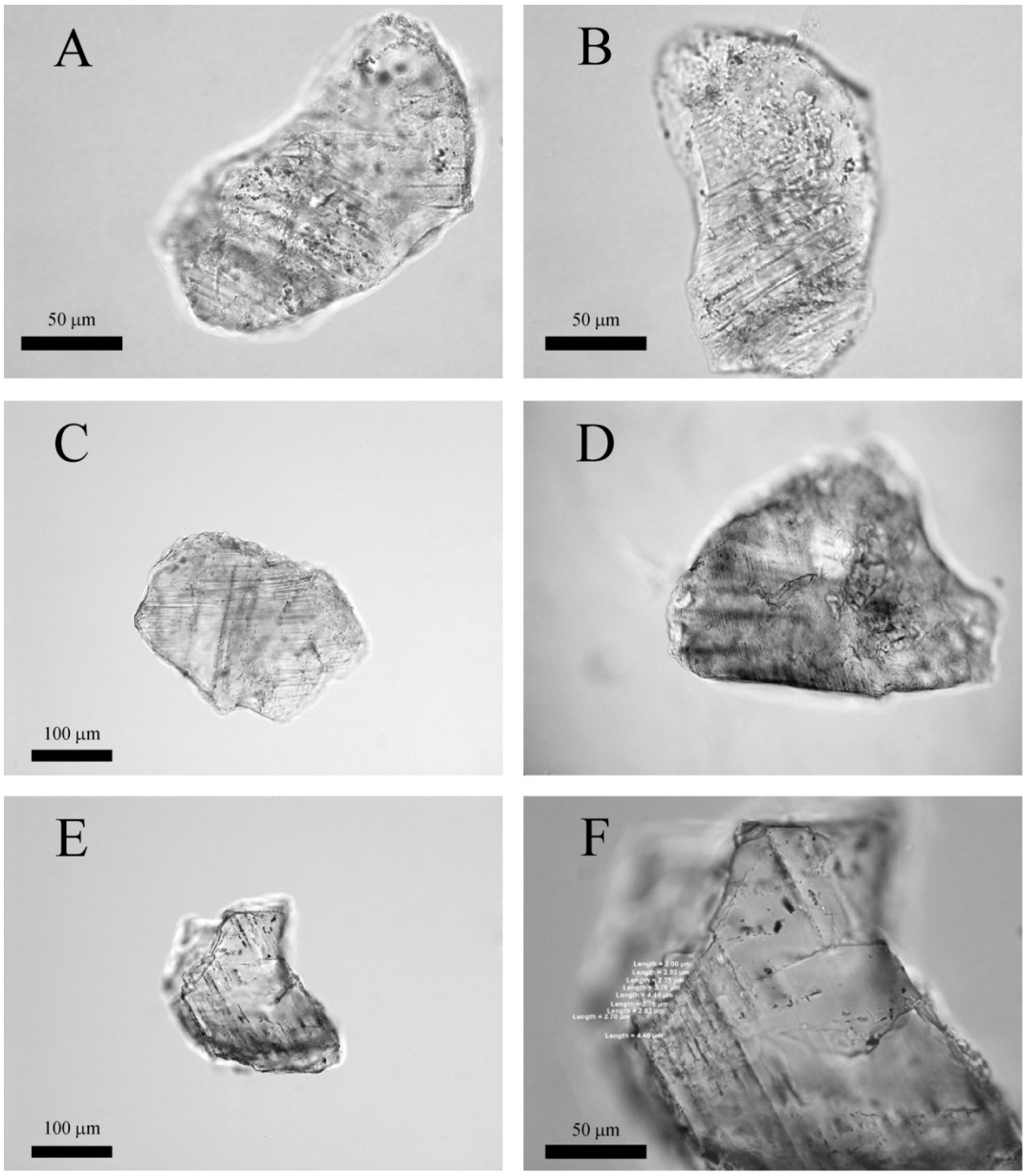

Figure A.2.3: Several quartz grains containing examples of what I am considering PMs. Figures 3A and 3B are the same sample with slightly different rotation and focal plane to show at least three sets of PMs. 3C contains at least two sets of PMs, at very low angle to each other in the current view. The sample in 3D also contains at least a single set of PMs; the grain is roughly 350 µm in longest dimension. 3E and 3F are the same grain. Spacing measurement locations are roughly visible on 3F. The average apparent PM spacing is 5.01 µm (3A and 3B), 4.85 µm (3C) and 3.26 µm (3E and 3F). The grains are mounted in immersion oil (n = 1.572) and photographed in plane-polarized light.

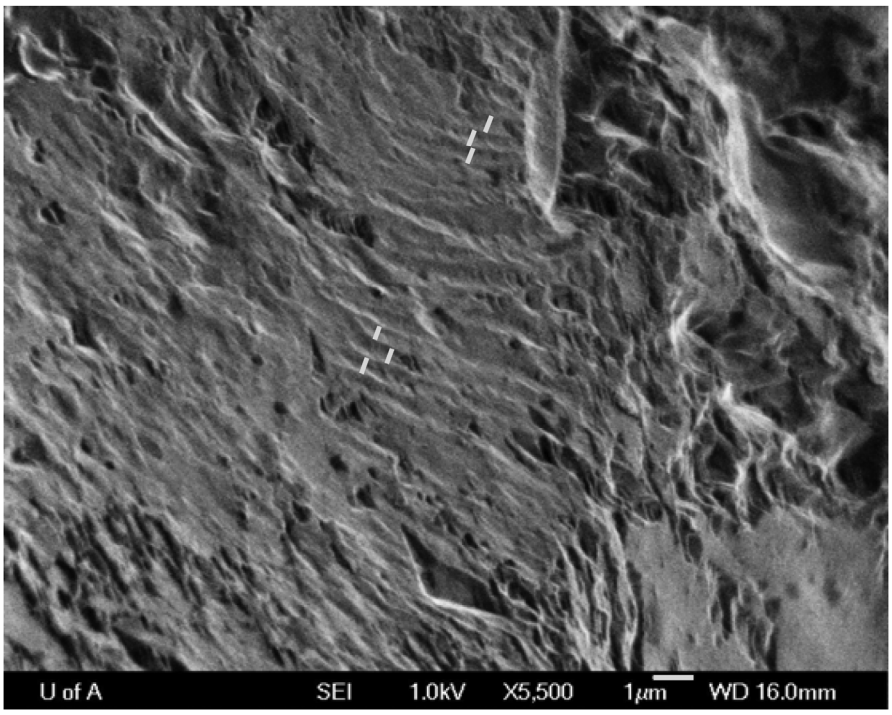

Figure A.2.4: An SEM image of the surface of a quartz grain etched in 49 % HF acid solution for 3 minutes; measurement locations are indicated in white. All grains observed using the SEM display patches, typically tens of micrometers across, of roughly parallel positive surface relief features. There is some variation in the separation and width of these striations, though they are generally <1 μm wide with adjacent striations in contact with each other. The average width of the striations in this sample is 404 nm.

A summary of the core points regarding the shock effects observed at the Whitecourt Crater are presented in Chapter 2. The Fe-Ni spherules (of which only three have been recovered to date) and meteorite dust provide additional evidence regarding the fate of the impactor. As discussed in Chapter 2 both are the result of the shock experienced by the impactor when it struck the surface.

The PMs observed in many of the quartz grains collected from the sand beneath the transient crater boundary appear to be of impact origin (Figure A.2.3). In particular, the nature and spacing of the PMs in measured samples correlate well with confirmed PDF-bearing quartz grains [e.g. Grieve *et al.* 1996; Gratz *et al.* 1996]. As the purpose of this project was simply to provide preliminary evidence of the presence of shocked quartz grains at the Whitecourt Crater further investigation is certainly warranted. More specifically, orientation data would provide critical supplementary data confirming, or refuting the impact origin of these features. It is also worth noting that the distal ejecta received less attention than the sediments beneath the transient crater boundary.

Many quartz grains were also recovered having slightly wavy and less well-defined parallel microstructures. Similar grains were observed within sand samples collected from one of the Paskapoo Formation sand outcrops at a road cut ~3 km north of the crater. These microstructures are likely of tectonic origin [e.g. Gratz *et al.* 1996] and were not included in the study.

The results of the HF etching are not addressed in Chapter 2. Gratz *et al.* (1996) etched their samples for several minutes in 30 % HF; it was thought reducing the exposure time would allow the use of a 49 % HF solution. In hind-site, there is a distinct possibility that the use of 49 % HF may have resulted in the fragmentation of any grains containing actual PDFs. These tiny fragments would easily have been lost in the fibrous filter paper and could explain the poor recovery rate for those samples. SEM images of the recovered grains did not reveal any deeply etched features [e.g. Gratz *et al.* 1996; Figure 1.4.1]. However, all of the analyzed recovered grains did show small patches of roughly parallel surface striations (Figure A.2.4). These striations occur on both curved and planar surfaces. The source of these striations is unclear and they are, at present, thought to represent either the results of conchoidal fracturing, or twinning. The vapor etched grain mount contained no PMs.

Appendix 3 – Geophysics:

Objective

The objective of this project is to complete seismic, resistivity, magnetic and gradiometric surveys at the Whitecourt Impact Crater and evaluate their potential usefulness.

Theory

It is beyond the scope of this appendix to provide a review for these topics. For information regarding seismic the reader could consult Steeples and Miller (1990), for Electrical Resistivity Tomography (ERT) consult Loke (2009), and for a general review of magnetic and gradiometric surveying see Lanza & Meloni (2006), particularly chapters 2 and 3.

Methods

At present, the seismic and ERT data are the result of a single profile passing through the deepest portion of the crater (Figure A.3.1). Grey Riddle, Femi Ogunsuyi and Xuefeng Duo from the University of Alberta performed the surveys and subsequent data analysis under the direction of Doug Schmitt. For the seismic survey, station spacing was 1 m over a distance of ~120 m. The seismic source was an 8 lb sledgehammer and there were three separate unstacked hammer strikes per shot point with a shot spacing of 3 m. A sampling rate of 62.5 μs for 0.75 s with 120 channels was used for the survey. The seismic line started at 11U 592014 5984294 (NAD83) and terminated at 11U 591905 5984332 (Figure A.3.1).

The ERT line was set up along the same profile as the Seismic line starting at 11U 591887 5984332 and terminating at 11U 591999 5984300. Survey points were set at 5 m intervals over a length of 125 m. Two surveys, using a Wenner and dipole-dipole array, were performed along the line. Figure A.3.1 illustrates the results of the dipole-dipole survey.

Using the GEM Systems GSM 19-TW and more sensitive 19-GW magnetometers, I conducted both magnetic and gradiometric surveys of the site. The

survey covered a roughly 100 m by 100 m region centered on the crater with additional data collected east of the grid (Figure A.3.2). The corners of the region are located at (region 11U, NAD83): 591990 5984367, 591996 5984274, 591896 5984271 and 591894 5984370. Figure A.3.2 illustrates the lines walked at various intervals running roughly parallel to the boundaries of the grid. Additional information regarding the survey is included in the Chapter 2.

To supplement the survey data, the strength of the magnetism of several meteorites was measured using a simple Vernier magnetic field sensor MG-BTA, with the help of Martin Connors of Athabasca University. The positive and negative magnetic poles were first identified on each sample after which it was mounted on a sled, designed to slide freely along a ruler, with a pole facing the detector. The strength of the magnetic field associated with strongest positive and negative pole was then measured at 2 cm and 1 cm intervals starting at a distance of 20 cm.

Data

The data are presented in Figures A.3.1 to A.3.3.

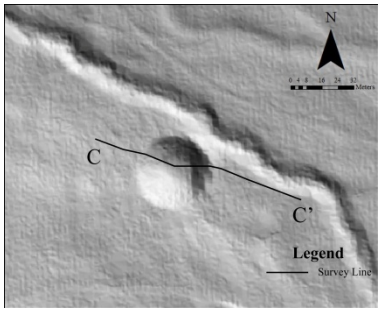

Figure A.3.1: The location (left) of the seismic and ERT survey line; the inverted resistivity data from the dipole-dipole survey (below). The crater rim is located at ~37 m and ~74 m (denoted with a 'V'). Due to the high conductivity of the soil, much of the signal travels through this region providing limited coverage at depth. As such, the results near the base of the figure, particularly at the corners, should be viewed with some skepticism.

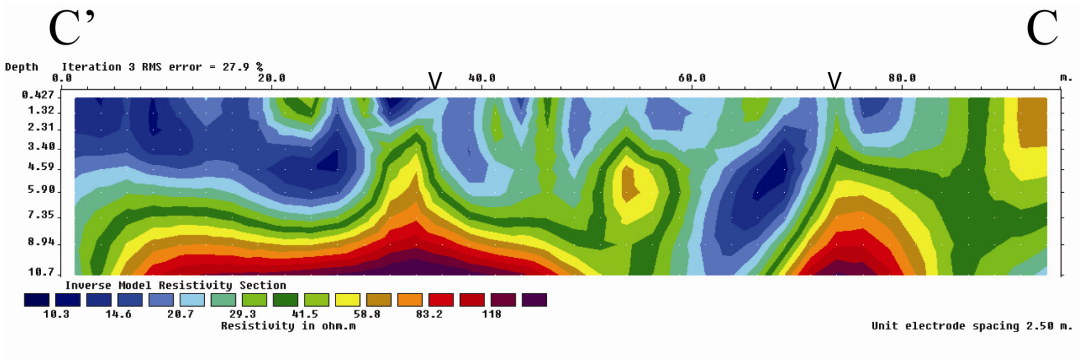

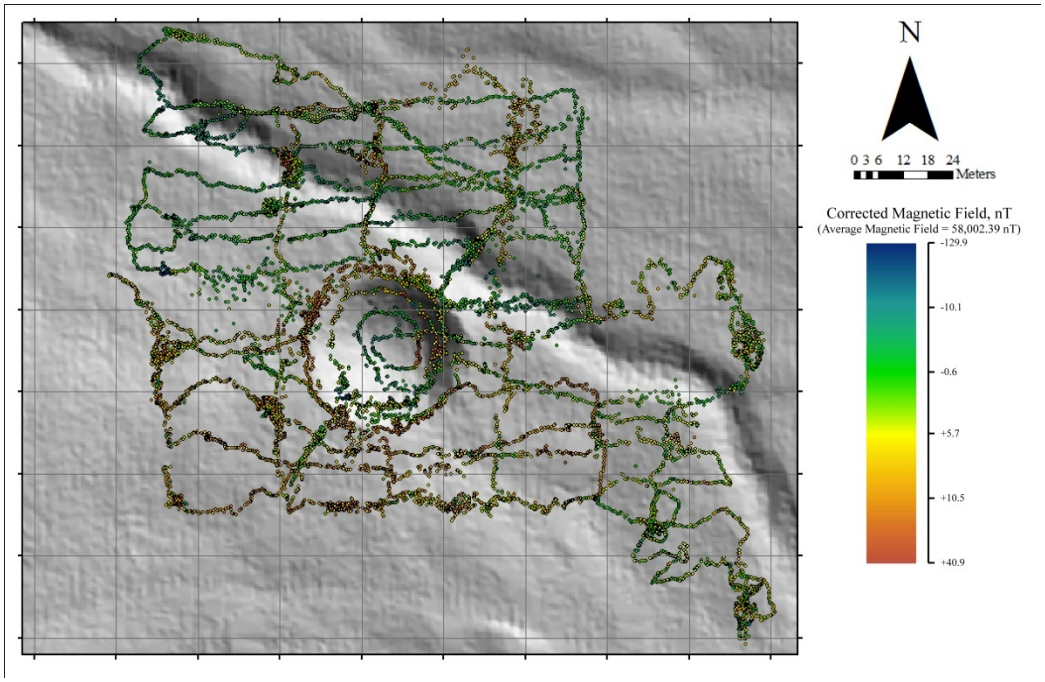

Figure A.3.2: A plot of the filtered data represented the points collected during two surveys conducted on and October 19 and November 14, 2008. Areas with high point counts represent sites with particularly dense foliage, or obvious anomalies. Unfortunately, the high point count could mask small anomalies depending on the interpolation techniques applied to the dataset (Figure 2.4.10).

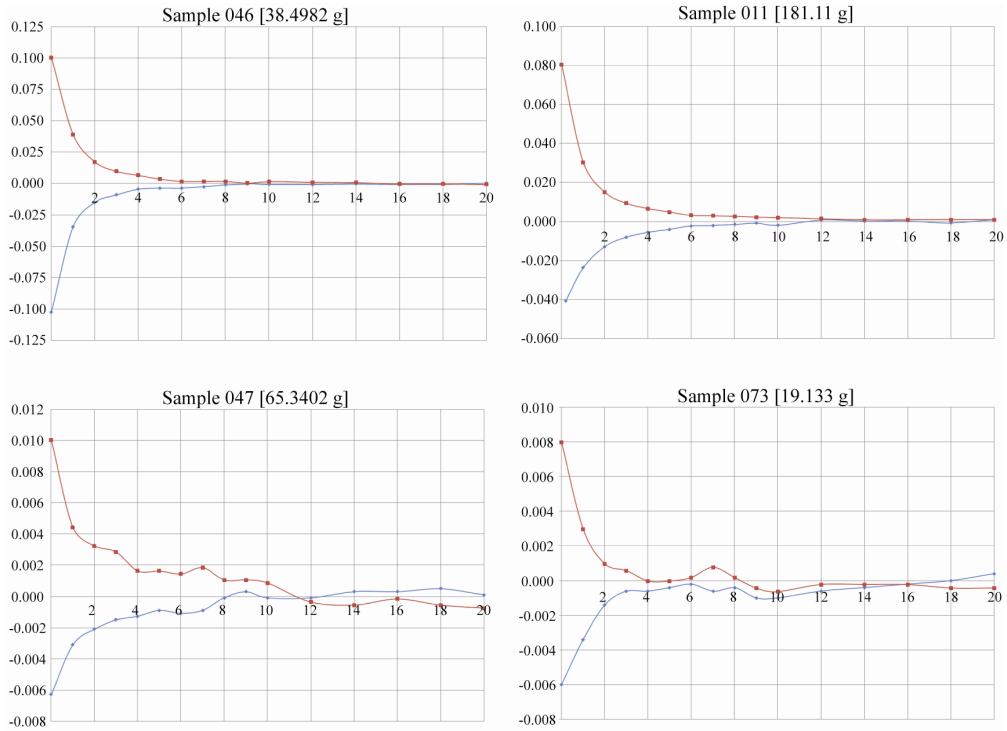

Figure A.3.3: The magnetic field measured for four of the Whitecourt meteorites. The samples were located on the crater rim (Sample 011), ~39.5 m from the crater center (Sample 047), ~62 m from the crater center (Sample 046), and ~32 m from the crater center (Sample 073). The vertical axis represents the magnetic field [mT] and the horizontal axis the distance from the sensor [cm].

Discussion

It was hoped that the seismic data would allow us to determine the near surface stratigraphy at the site. Unfortunately, background noise significantly reduced the quality of the data. As such, the survey provided little insight into the local stratigraphy. Additional seismic surveys were not attempted.

The results from the ERT survey correlate well with the borehole data collected at the site obtained along a similar line in Figure 2.4.2. It should be noted that the inverted resistivity on the plot is not the true resistivity because the survey was conducted on a highly conductive soil – 10 Ω·m to 20 Ω·m [Grey Riddle, *personal communication*]. In general, the results outside the crater rim indicated an expected increase in resistivity with depth and limited lateral variation. Within the crater there is an increase in heterogeneity. This is a reflection of the different properties of the mixed sediments that comprise the crater fill. The crater fill is composed primarily of damp diamict with discrete unconsolidated fine sand lenses - the largest observed sand lens being ~65 cm thick. It is unclear what is responsible for the large conductive zone along the west crater wall. The ERT data does reveal a somewhat bowl-shaped feature beneath the crater. It is possible that this feature delineates the distribution of the subsurface impact-affected materials, though more borehole data would be required to confirm this.

The critical elements of the magnetic survey are discussed in Chapter 2. The purpose of the additional measurements of the magnetism associated with the meteorites was to determine if they posses consistent values. It is clear from plots in Figure A.3.3 that there is a large variation, of at least two orders of magnitude, in the observed magnetic field of some of the measured samples. Sample 046, the most strongly magnetic sample, is essentially a magnetic dipole with the positive and negative poles at opposing ends of the meteorite. The other samples show more complex field structures with as many as seven distinct poles. It does not appear that terrestrial weathering is responsible for these variations, and the lack of fusion crust precludes the possibility of thin surficial remagnetised zone related to ablation [e.g. Kohout *et al.* 2004]. It seems most likely that the variations in the measured field strength relates to magnitude of shock experienced by each sample either when it stuck the terrestrial surface, or during an impact event prior to its arrival on Earth [e.g. Gattacceca *et al.* 2007]. In addition, the complexity of the magnetic field structure in the remnant magnetism of several samples also suggests that the bulk of the magnetism observed in the Whitecourt meteorites is of

extraterrestrial origin. Detailed magnetic studies of the meteorites and subsequent forward modeling of the survey results to determine how the magnetometer would respond to Whitecourt meteorites of various sizes and depths extend beyond the scope of this thesis.

Conclusions

The ERT survey, in combination with the borehole data, and magnetic survey were both revealing. Additional ERT surveys, along different trends, could effectively provide a 3D view of the structure by mapping the distribution of impact-affected sediments. The preliminary magnetic investigations of several Whitecourt meteorites suggest that they too have more to add to the overall dataset. In particular, forward modeling of the magnetic survey based on the magnetic properties of the meteorites, and additional surveys, now that the major anomalies have been removed, may provide further insights into the site. Unfortunately, the effectiveness of seismic investigations of the crater is limited.

Appendix 4 - Ballistics:

Objective

The objective of this project is to determine approximate ejection velocities (for various ejection angles) of five Whitecourt meteorites. A comparison of flight trajectories in a vacuum and in the presence of the atmosphere, taking into account atmospheric drag, will be made to determine the significance of atmospheric interaction at an impact crater of this scale.

Theory

Assuming the distribution of meteorites is a result of impact spallation, in which case meteorite fragments spall off the main mass during impact; it is possible to estimate the ejection velocities of the meteorites based on their physical properties and distance from the crater centre. Two scenarios will be considered for plotting the flight path of the five meteorites: 1. Flight neglecting atmospheric interaction; 2. Flight accounting for atmospheric interaction. The first scenario represents the simplest and crudest approximation of the meteorites' trajectories. Using an admittedly simplified approach to modeling atmospheric interaction, the second scenario should nevertheless provide a more accurate representation of the meteorites' trajectories. The techniques used to account for the atmospheric influence on the meteorites' trajectory are meant to provide approximate values only; as the goal of this project is simply to provide a comparison of the approximate velocities in each scenario, the techniques used should be adequate. In each case the determination of the final position will be determined through iterative finite difference calculations ending once the vertical position, initially at y = 0 m, intersects y = 0 m after traveling though a single maximum value.

In each case the flight of the meteorite will be divided into vertical, y, and horizontal, x, components. The position of the meteorite at time, t in seconds [s], based on classical kinematics is given by:

$$x_f - x_i = (v_i \cos\theta_i)t \qquad [1]$$

$$y_f - y_i = (v_i \sin\theta_i)t - \frac{1}{2}gt^2 \qquad [2]$$

where x_i and x_f represent the initial and final horizontal positions in meters [m] respectively over some time interval Δt [s]; y_i and y_f are the vertical positions [m], v_i is the

initial velocity in meters per second [m/s], θ_i is the ejection angle in radians, and g is Earth's gravitational acceleration – taken here as 9.81 m/s^2. Taking the first derivative, with respect to time, of [1] and [2] allow the determination of the initial horizontal and vertical components of the velocity vector of the meteorite such that:

$$v_{xi} = v_i \cos\theta_i \quad [3]$$

$$v_{yi} = v_i \sin\theta_i - gt \quad [4]$$

Where atmospheric interaction is neglected the horizontal velocity, v_x, remains constant and the vertical component, v_y, varies over a given time interval as:

$$v_{yf} = v_{yi} - gt \quad [5]$$

Once atmospheric effects are taken into consideration the effects of drag must be introduced into the calculations. The drag force, F_d measured in Newtons [N], represents the force applied to a body as it travels through a fluid and is defined as:

$$F_d = \frac{1}{2} C_d \rho_f A v^2 = m a_d \quad [6]$$

where ρ_f is the mass density of the fluid in kilograms per cubic meter [kg/m^3], A is the projected area of the object in square meters [m^2], v is the velocity of the object [m/s], m is the mass of the object in kilograms [kg], and a_d is the deceleration of the object [m/s^2]. C_d is the drag coefficient, a dimensionless number that represents the amount of drag, or resistance, a body experiences while traveling through a fluid.

The drag coefficient provides the greatest uncertainty in the calculation and must be determined experimentally (Figure A.4.1). In Figure A.4.1 there are two distinct flow regimes for the cylinder and the sphere separated by the region plotted using dashed lines. The laminar flow regime occurs at lower Reynolds number values, R_e, while the turbulent flow regime occurs at higher R_e values, where C_d is significantly lower. The Reynolds number is a dimensionless value representing the ratio of inertial forces to viscous forces. It is also worth noting that once an object enters the turbulent flow regime C_d is no longer strongly dependant on R_e, but is instead controlled by the object's velocity. For meteoroids transiting the atmosphere little study has been done for centimeter- to metre-scale bodies at high R_e values [>10^5, H. J. Melosh *personal communication*]. For modeling meteoroid flight in the lower atmosphere C_d = 0.5 is often used [e.g. Passey & Melosh, 1980; Melosh & Collins, 2005].

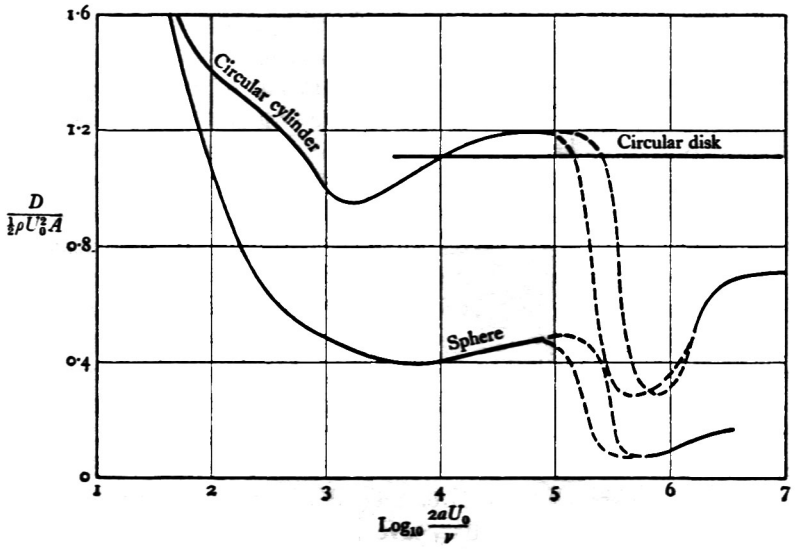

Figure A.4.1: The drag as measured along the unit axial length of a circular cylinder ($A = 2a$), on a sphere ($A = \pi a^2$), and on a circular disk normal to the stream ($A = \pi a^2$), all of radius a. The dashed curves represent results obtained in different wind tunnels. [Batchelor, 1967; p. 341]. The vertical axis represents C_d, where $D = F_d$, $U_0 = \upsilon$ and ν is the dynamic viscosity of air. The horizontal axis represents the log(R_e).

Table A.4.1 provides the specific details of the samples being considered in this project. Even at 10 m/s all of the samples have R_e values very near to the transition from the laminar to turbulent flow regimes indicated for both the sphere and the cylinder in Figure A.4.1. It is expected that this transition would occur at a lower R_e value for meteorites due to their irregular shape and because they are likely spinning; the effects of spin/rotation will not be addressed here. The C_d value of 0.5 does not seem unreasonable; however, It soon became apparent that this value was too high to be used for this project and was replaced with the C_d = 0.25 in accordance with the value measured for the sphere in Figure A.4.1. R_e is determined using:

$$R_e = \frac{2r_0 U_0}{\nu} \qquad [7]$$

where r_0 is the average radius of the meteorite in [m], U_0 is its velocity [m/s] and ν is the dynamic viscosity of air (1.74 x 10^{-5} kg/(m·s) at 0°C).

Unlike the airless situation, both the horizontal and vertical components of the meteorite's velocity experience deceleration due to drag in the presence of the atmosphere. This is most strongly dependent on the meteorite's velocity according to [6]. One implication is that the meteorite experiences the greatest drag force along its upward trajectory. A final consideration must also be given to the terminal velocity, υ_t [m/s], of

the meteorite along the vertical component of its downward trajectory. This can be calculated using:

$$\upsilon_t = \sqrt{\frac{2mg}{\rho_f A C_d}} \quad [8]$$

Where m is the mass of the object [kg] and ρ_f is the mass density of the fluid [kg/m^3]. Since the crater formed at an elevation of ~910m, the mass density of the atmosphere, the host fluid, must also be determined using:

$$\rho_f \sim \rho_0 e^{\frac{-Z}{H}} \quad [9]$$

where ρ_0 is atmospheric mass density at sea level (1.29 kg/m^3 at 0°C), Z is the altitude [m] and H is the scale height [m] which is essentially the vertical distance upwards from the planet's surface over which the atmospheric pressure drops by a factor of $\boldsymbol{e}$ – taken to be 8,000 m. Values for υ_t are presented in Table A.4.1. Once the meteorite reaches υ_t along its downward trajectory $\upsilon_y = \upsilon_t$ and is held constant until it reaches the ground.

A minimum ejection angle of 50° was used as a means of neglecting possible interactions with the ejecta curtain formed during impact as this could have a significant effect on limiting the range of an ejected meteorite. The potential meteorite/ejecta interaction (a phenomenon that is observed at the site) is beyond the scope of this project.

Calculations were performed on a spreadsheet created in Microsoft Excel™. Two sets of calculations were performed for each sample using Δt = 0.5 s and Δt = 0.25 s to determine if the iterative process was systematically over- or under-estimating the values.

Table A.4.1: The physical properties of each sample, associated R_e value at specified velocity, distance from the crater and terminal velocity.

Sample	Mass [kg]	A [m^2]	r_0 [m]*	R_e [10 m/s]	R_e [150 m/s]	R [m]**	υ_t [m/s]
10	0.855150	7.19E-03	0.09600	1.11E+05	1.66E+06	18	90.07
93	0.041479	1.14E-03	0.03700	4.26E+04	6.39E+05	27	49.85
179	0.015970	5.96E-04	0.01375	1.58E+04	2.38E+05	175	42.76
181	0.368363	3.38E-03	0.06900	7.95E+04	1.19E+06	65	86.21
159	0.146400	1.80E-03	0.04900	5.65E+04	8.47E+05	48	74.46

* Average of longest and shortest dimensions through center of the sample's projected area
** Distance from crater center

Data

The data are presented in Table A.4.2 and Figure A.4.2.

Table A.4.2: This table summarizes the results of the calculations in which atmospheric effects are taken into account. The flight time, t_f [s], represents the final time interval with a positive altitude. The initial velocity, v_i [m/s], is the velocity required to launch the meteorite a distance, R [m], from the center of the crater. Calculations using time intervals of $\Delta t = 0.50$ s and $\Delta t = 0.25$ s are included.

		Sample				
		10	**93**	**159**	**179**	**181**
$\Delta t = 0.50$ s	v_i (50°)	12.00	15.45	20.95	60.40	24.65
	t (50°)	2.50	3.00	3.50	7.50	4.50
	v_i (65°)	14.05	18.30	24.50	75.40	28.70
	t (65°)	3.00	3.50	5.00	9.00	5.50
	v_i (80°)	21.90	28.80	38.25	140.00	44.72
	t (80°)	5.00	5.50	7.50	12.00	8.50
$\Delta t = 0.25$ s	v_i (50°)	12.72	16.24	21.75	61.20	25.45
	t (50°)	2.25	2.75	3.50	7.50	4.25
	v_i (65°)	14.65	18.80	25.05	72.50	29.30
	t (65°)	3.00	3.50	4.75	9.00	5.50
	v_i (80°)	22.46	29.45	38.90	130.00	45.40
	t (80°)	4.75	5.50	7.50	12.50	8.50

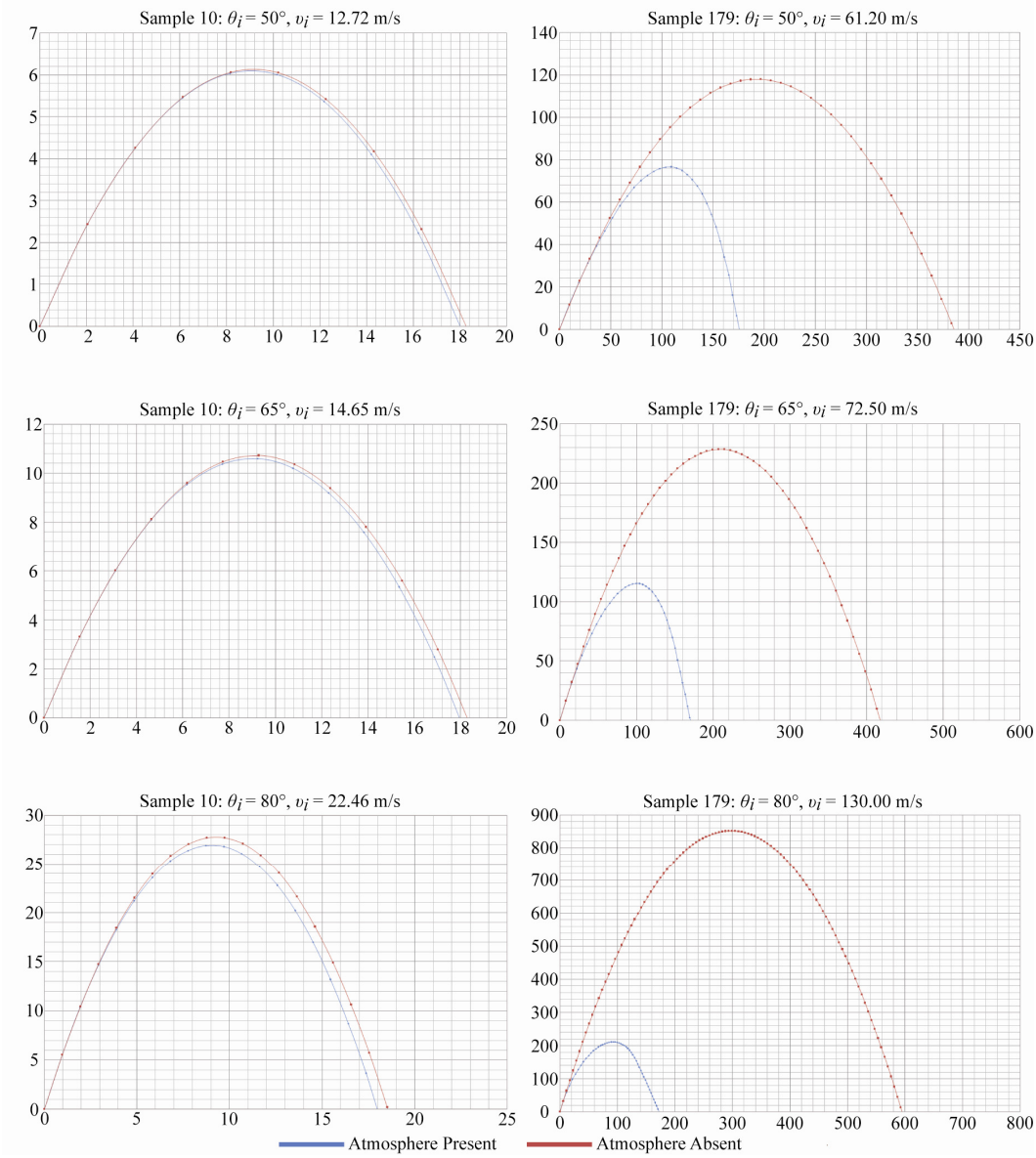

Figure A.4.2: Calculated trajectories for samples 179 and 10 using $\Delta t = 0.25$ s. The vertical axis represents height [m] and the horizontal axis represents range [m].

Discussion and Conclusions

It is clear in the approximations (Table A.4.2 and Figure A.4.2) that atmospheric influence increases with decreasing projectile mass and increasing projectile velocity. It is clear from the results that for meteorites having masses several tens of grams or less, atmospheric drag must be taken into account when calculating their ejection velocities. The vast majority of meteorites recovered from R >100 m at the Whitecourt Crater fall into this category. For meteorites having masses approaching and exceeding 1 kg, the

atmosphere's influence is greatly reduced. Possible ejection velocities for the samples range from ~12 m/s to ~140 m/s in the presence of the atmosphere, a small fraction of the original impact velocity (likely between ~8 - 10 km/s - Chapter 2 and Appendix 5).

Appendix 5 – Impact Parameters:

Objective

The objective of this project is to use observations at the Whitecourt Crater and recent models to attempt to place constraints on the impact parameters, including impactor trajectory, velocity and diameter, required to form the crater. The core focus of this entry will be to use observations and modeling to determine the approximate radius of the impactor at the time of impact and use this radius to place constraints on properties of the Whitecourt meteoroid immediately prior to atmospheric entry and its trajectory through the atmosphere.

Theory

Several critical impact parameters are presented in Chapter 2, particularly in Section 2.5. There I conclude that the impactor struck the surface at an angle of 40° to 55° to horizontal while traveling roughly 8 km/s to 10 km/s. It is unlikely that an iron meteoroid of the size required to form the Whitecourt Crater would be slowed to velocities much less than 8 km/s at the proposed impact angles, taking the minimum encounter velocity between a meteoroid and Earth to be 11.2 km/s [Melosh, 1989]. A combination of two models, both of which treat the meteoroid as a sphere, will be used to first determine the size of the iron impactor required to form the crater, and second to determine a range of impact parameters prior to atmospheric entry, during atmospheric transit and at the time of impact. The results of the modeling will provide a theoretical basis for my conclusions.

To determine the approximate size of the meteoroid at the time of impact I will use a technique similar to that of Kenkmann *et al.* (2009) for the recently formed Carancas (Peru) impact crater. In this project impact cratering scaling laws, laws that relate the various features of impacts, are used to calculate the possible radii for the impactor and the energy required to form the observed crater. Here I will be using scaling laws based on the theoretical analyses of cratering mechanics by Holsapple and Schmidt (1987), Housen *et al.* (1983) and Holsapple (1993) [for review see Holsapple, 1993]. In particular, the ratio of the final transient crater radius, R, to the radius of the

impactor at the time of impact, a, can be determined using the general equation from Holsapple & Housen (2007):

$$\frac{R}{a} = K_1 \left[\frac{ga}{U^2} \left(\frac{\rho}{\delta} \right)^{\frac{2\nu}{\mu}} + \left(\frac{Y}{\rho U^2} \right)^{\frac{2+\mu}{2}} \left(\frac{\rho}{\delta} \right)^{\frac{\nu(2+\mu)}{\mu}} \right]^{\frac{-\mu}{2+\mu}} \quad [10]$$

where K_1, ν and μ, are unit-less scaling coefficients. g is the gravitational acceleration of the target, U is the normal component of the impactor's velocity, ρ is the mass density of the target, δ is the mass density of the impactor, and Y is the cohesive strength of the target material; all values are reported in SI units. The following material properties were used in the calculations: δ = 7,800 kg/m^3, R = 14.5 m (the diameter of the transient crater is roughly 29 m), Y = 1,000 Pa and ρ = 2,000 kg/m^3. The values for Y and ρ are for water saturated sand [Kenkmann *et al.* 2009], which I am using to approximate the properties of the target materials at the Whitecourt Crater. The values for U are obtained from impact velocities of 6 km/s, 8 km/s and 10 km/s for 40° and 55° impact angles.

There are a number of limitations to this model, with respect to the Whitecourt Crater, that should be mentioned. Three areas of uncertainty I feel are important include the role of layering, scaling parameter values and porosity. It is clear that there are at least two different units affected by the impact, glacial till and unconsolidated massive fine sand, and this model does not address target material layering. The scaling coefficients, which must be determined experimentally, have only been determined for a small number of materials. As there is no data for the dominant target sediments at the Whitecourt Crater, glacial till (the till is damp, though not water-saturated, and contains roughly equal parts clay, silt and very-fine sand), I will be using what I believe is the closet available analog: water saturated sand. For water saturated sand K_1 = 0.93, ν = 0.4 and μ = 0.55 [Holsapple & Housen, 2007]. While the porosity of the target sediments at the Whitecourt Crater have not been determined, it is likely that it played a significant role in determining the final crater size. At present, the effect of porosity in the impact cratering process is not well-understood. However, it is clear that increasing porosity can significantly alter the crater forming processes that occur in targets with little or no porosity [e.g. Housen & Holsapple, 2003; Wünnemann *et al.* 2006 and references therein]. This is accounted for, in part, by the scaling coefficients, though this does not address possible changes in the formation processes themselves. Please see the review papers for additional discussion regarding the physical meanings of the scaling coefficients and the role of the impact angle and momentum.

Once possible radii for the meteoroid at the time of impact are determined, the second model can be applied. Here I use a program written by H. J. Melosh, which models the atmospheric transit of a meteoroid. The process involves varying three of the initial variables: initRadius, the radius of the meteoroid when it enters the atmosphere, entryVel, the velocity of the meteoroid when it first enters the atmosphere and entryAng, the angle from horizontal at which the meteoroid enters the atmosphere. These values are varied until the end results closely match a series of predetermined values. In particular, I am interested in the velocity and impact angle at the time of impact as determined from observation, and the meteor's radius at the time of impact calculated using [10]. While these solutions are necessarily non-unique, they should provide a reasonable estimate of the parameters in question. The text of the notebook is included, with permission, at the end of this appendix entry. I have made one modification to the notebook to reflect the fact that the impact occurs at an elevation of 910 m. A comment regarding this is included in the notebook immediately preceding the formula and is initiated with ***. As the notebook was written using Mathematica™, application of the program will require some knowledge of the software. Explanations are provided within the notebook and will not be included here.

Data

The results of the calculations are presented in Table A.5.1. The target variables include the radius of the meteoroid calculated using [10] and the velocity (impact velocity) of the meteor at the time of impact, in addition to the impact angle as determined from observations at the crater. The input variables represent the radius and velocity (entry velocity) of the meteoroid upon entering the atmosphere, in addition to the entry angle. In the program atmospheric entry is initiated at an elevation of 200 km. The input variables listed provide one set of results for each scenario that closely match the target variables. The results list the values obtained using the program. Additionally, I have provided the kinetic energy and momentum of the meteoroid at the time of impact.

Table A.5.1: This is a summary of the results of the calculations using [10] and the program.

	Scenario 1	Scenario 2	Scenario 3	Scenario 4	Scenario 5	Scenario 6
Target Variables:						
Radius [m]	0.3844	0.3281	0.2902	0.3364	0.2872	0.2539
Velocity [m/s]	6000	8000	10000	6000	8000	10000
Angle [°]	40	40	40	55	55	55
Input Variables:						
Initial Radius [m]	0.425	0.41	0.43	0.36	0.35	0.355
Entry Velocity [km/s]	8.75	12.3	15.75	8.35	11.8	15.2
Entry Angle [°]	40.3	41.1	41.5	55.08	55.6	55.85
Results:						
Final Radius [m]	0.3853	0.3288	0.2938	0.3311	0.2895	0.2532
Impact Velocity [m/s]	6006.44	7974.74	9981.01	5936.32	7999.58	9963.98
Impact Angle [°]	39.96	39.93	40.00	54.98	54.40	54.80
Transit Time [s]	35.49	25.24	19.67	29.17	20.74	16.13
Initial Mass [kg]	2508.13	2251.83	2597.70	1524.37	1400.84	1461.73
Final Mass [kg]	1868.33	1160.90	828.56	1185.65	792.63	530.40
Max. Stagnation Pressure [bar]	195	340	530	195	340	530
Kinetic Energy [J]	3.37E+10	3.69E+10	4.13E+10	2.09E+10	2.54E+10	2.63E+10
Kinetic Energy [kT TNT]	8.06E-03	8.82E-03	9.86E-03	4.99E-03	6.06E-03	6.29E-03
Final Momentum [kg·m/s]	1.12E+07	9.26E+06	8.27E+06	7.04E+06	6.34E+06	5.28E+06

Discussion and Conclusions

There is, admittedly, significant uncertainty in the modeled results. I believe the largest uncertainty lies in the calculation of the meteoroid radii using equation [10]. The current lack of accurate values for the mass density and cohesive strength of the target materials and the use of the scaling coefficients K_1, v and μ for water-saturated sand to represent the target material are the primary sources of uncertainty in this instance. For example, using the scaling coefficients, cohesive strength and mass density for dry sand, and considering an impact velocity of 10 km/s at an impact angle of 55° doubles the radius of the impactor striking water-saturated sand.

Based on the results of this project it is possible to outline a possible impact scenario for the Whitecourt Crater. It is evident from the modeling that impact velocity could not have been much lower than 8 km/s, again taking the minimum encounter velocity to be 11.2 km/s [Melosh, 1989]. Impact velocities of 6 km/s, at impact angles of 40° to 55°, require entry velocities well below 11.2 km/s, and can theoretically be ruled out. Ignoring scenarios 1 and 4, constraints can now be placed on the properties of the meteoroid at the time of atmospheric entry and at impact. Based on the modeling, at the time of entry the Whitecourt meteoroid had a radius of 35 cm to 40 cm, was traveling 12

km/s to 16 km/s, and entered at an angle of 41° to 56° to surface of Earth. On reaching the target surface, the meteor had a radius of 25 cm to 33 cm. Observations place the impact velocity at 8 km/s to 10 km/s, and the impact angle at 40° to 55°.

Another important result obtained from the modeling involves the maximum stagnation pressure experienced by the incoming meteoroid. It is proposed in Section 2.5 that the meteoroid remained essentially intact while traversing the atmosphere. This implies that the stagnation pressure did not exceed the yield strength of the meteor [e.g. Passey & Melosh, 1980]. Petrovic (2001) concludes that the average compressive strength of iron meteorites is ~430 MPa, or 4.3 kbar and notes that the actual catastrophic disruption of an incoming meteoroid may occur at pressures as much as a factor of ten below this. In particular, it should be noted that the overall compressive strength decreases with increasing meteor size [Weibull, 1951]. The results of the modeling place the maximum stagnation pressure at ~530 bar at 10 km/s, though it drops to ~340 bar at 8 km/s. These results, in addition to the relatively small size of the meteoroid, suggest that it could have remained intact during atmospheric transit, concluded based on observations of the crater and associated meteorites.

METEORITE ENTRY

Notebook for computing the trajectory and temperature of a meteorite entering the Earth's atmosphere.

Use standard meteor ablation theory and trajectory analysis from Chapter 11 of my book to compute the trajectory of a meteorite entering the Earth's atmosphere. The drag coefficient used is my newly determined formula based on Crowe's paper, that behaves correctly from rarefied gas flow to the slow Stokes flow regime. Also, the heat transfer coefficient is determined from the Nusselt number and drag coefficient, as determined for my KFIX computation.

The Crowe drag formula is very complex and depends on two other variables, the ratio of specific heats of the gas, gamma (gamma = 1.4 for diatomic air), and the ratio between the temperature of the particle, Tp and that of the gas Tg. I will call this ratio tratio = Tp/Tg, but usually set it equal to unity.

gamma=1.4;
prandtl=0.72;
tratio=1;

Define some parameters that describe the Earth and its atmosphere

gearth=9.8;
eRadius=6371.;
rho0=1.2;
hscale=8.;
eta=1.7*10^-5;
csound=300.;

now some parameters that describe the infalling meteor (mks units, heat capacity is in J/kg-K). Variable a0 is the initial radius, zeta is the ablation coefficient in J/kg and vcrit is the critical velocity in m/sec below which ablation is unimportant. ablateCH is the ablation coefficient, basically the efficiency with which friction heat is transferred to the surface of the meteorite. Note that this formulation neglects mass loss by radiation, which can be very important for small particles!

rhopart=7800.;
initRadius=1.0;
zeta=5*10^6;
vcrit=3000;
ablateCH=0.02;

Define the initial conditions of the entering particle; its altitude, velocity and angle of entry. The coordinate system used will be altitude above the surface, z, downrange distance x, and the velocity in these directions. All units are in mks to be consistent and angles are in radians, so some conversions may be necessary.

The actual user inputs are velocity in km/sec, entry angle from the horizontal in degrees and the intial altitude in km. The initial downrange distance is assumed to be zero.

entryVel=14;
entryAng=40;
initAlt=200.;
initMass=(4*Pi/3)***rhopart*initRadius**^3

Define a few useful numerical conversion factors

degrad=Pi/180.;
radeg=1/**degrad**;

The shape factor relates the cross-sectional area of the meteoroid to its mass. It equals about 1.2 for spheres

shapeF=Pi/(4*Pi/3)^(2/3);

the density of the air as a function of height, mach and reynolds numbers are:

rho[*z*_]:=**rho0***Exp[-z/(1000***hscale**)]
mach[*v*_]**:=***v*/**csound**
renum[*v*_,*z*_,*mass*_]:=2*Sqrt[**area**[*mass*]/Pi]***rho**[*z*]**v*/**eta**

The drag relation previously derived in another notebook, based on the 1967 paper by Crowe and our own adaptations to it is given by:

cdragINC[*re_*]:=(24/*re*)*(1+0.25**re*^0.5)+.25
cdrag[*re_,machnum_*]:=2+(**cdragINC**[*re*]-2)*Exp[-3.07*Sqrt[**gamma**]*(*machnum*/*re*)*gfunc[*re*]]+(**hfunc**[*machnum*]/(Sqrt[**gamma**]**machnum*))*Exp[-*re*/(2**machnum*)]

For this function define a pair of auxiliary functions:

gfunc[*re_*]:=10^(2.5*((*re*/312)^0.6688)/(1+(*re*/312)^0.6688))
hfunc[*machnum_*]:=4.6/(*machnum*+1)+1.7*Sqrt[**tratio**]

I will also need an expression for the Nusslet number for heat transfer as a function of re and m as well. Use the form derived in the last few days, a modification of the Kavanau equation:

nu0[*re_*]:=2+0.459*(*re*^0.55)*(**prandtl**)^0.33
nuP[*re_,machnum_*]:=**nu0**[*re*]/(1+3.42*(**mmod**[*machnum*]/(*re***prandtl**))***nu0**[*re*])
mmod[*machnum_*]:=*machnum*/(1+3.42**machnum**((**gamma**+1)/(8***gamma**)));

Finally, apply this to the computation of the friction factor alpha, that describes the fraction of the total power lost, given by the drag force*velocity, that goes into the droplet.

recSmp[*re_,machnum_*]:=(Sqrt[**prandtl**]+(*machnum*/*re*)*2***gamma**/(1+**gamma**))/(1+*machnum*/*re*)
alpha[*re_,machnum_*]:=8***nuP**[*re*,*machnum*]***recSmp**[*re*,*machnum*]/(**gamma***re***prandtl***cdrag**[*re*,*machnum*])

When ablation occurs the mass of the incoming meteoroid decreases with time. Because the cross sectional area is thus variable, it must be constantly recomputed. Define a function that returns an area based on the mass and a shape factor shapeF:

area[mass_]:=**shapeF***(*mass*/**rhopart**)^(2/3)

Define some auxiliary functions needed for the trajectory integration. Note that this version substitutes the ablation coefficient for the more exact computation using alpha for the frictional heat transfer to the meteoroid

ablate[*v_*]:=If[*v*>**vcrit**,(*v*^2-**vcrit**^2)/*v*^2,0]
massloss[*v_,z_,mass_*]:=(0.5/**zeta**)***ablateCH***rho**[*z*]***area**[*mass*]***ablate**[*v*]**v*^3
dragForce[*v_,z_,mass_*]:=0.5***rho**[*z*]***area**[*mass*]***cdrag**[**renum**[*v*,*z*,*mass*],**mach**[*v*]]**v*^2
dragAcc[*v_,z_,mass_*]:=**dragForce**[*v*,*z*,*mass*]/*mass*

The equations of motion are here defined as in my book on impact cratering, chapter 11. This is the standard form for meteoroid entry, as a set of coupled first order differential equations.

meteorEqs:={

v'[*t*]==-**dragAcc**[**v**[*t*],**z**[*t*],**m**[*t*]]+**gearth***Sin[**θ**[*t*]], **θ'**[*t*]==(**gearth**/**v**[*t*]-**v**[*t*]/(**z**[*t*]+**eRadius***1000))*Cos[**θ** [*t*]],**z'**[*t*]==-**v**[*t*]*Sin[**θ**[*t*]],**x'**[*t*]==**v**[*t*]*Cos[**θ**[*t*]]/(1+**z**[*t*]/(**eRadius***1000)),
m'[*t*]==-**massloss**[**v**[*t*],**z**[*t*],**m**[*t*]],

v[0]==**v0**,**θ[0]== θ0**,**z**[0]==**z0**,**x**[0]==**x0**,**m**[0]==**m0**
}

Now set the initial conditions for the integration

v0:=1000***entryVel**
θ0:=**degrad***entryAng**
z0:=1000***initAlt**
x0:=0
m0:=**initMass**

Estimate the maximum time of integration as the free fall time from the initial altitude

maxtime=Sqrt[2***z0**/**gearth**]
trajectory=NDSolve[**meteorEqs**,{**v**, **θ**,**z**,**x**,**m**},{**t**,0,**maxtime**}]

get the actual time of impact from these interpolation formulas

altitude[*t_*]:=**z**[*t*]/.**trajectory**[[1]]

***I'm modifying the impact time (impacTime) by changing the final altitude to 910 m to reflect the elevation of the Whitecourt impact crater – where I've changed it to **altitude**[*t*]==910 below.

impacTime=t/.FindRoot[**altitude**[*t*]==910,{*t*,**maxtime**,0,**maxtime**}][[1]]
impactVelocity=v[**impacTime**]/.**trajectory**[[1]]

```
Plot[radeg* θ[t]/.trajectory,{t,0,impacTime},AxesLabel→{"time,sec","trajectory angle, degrees"},PlotRange→All]

Plot[z[t]/1000/.trajectory,{t,0,impacTime},PlotRange→All, AxesLabel→{"time, sec","altitude, km"}]

Plot[v[t]/1000/.trajectory,{t,0,impacTime},PlotRange→All, AxesLabel→{"time, sec","velocity,
km/sec"},AxesOrigin→{0,0}]

ParametricPlot[{v[t]/1000,z[t]/1000}/.trajectory,{t,0,impacTime},PlotRange→All,AxesLabel→{"velocity,
km/sec","altitude, km"},AspectRatio→1]

ParametricPlot[{x[t]/1000,z[t]/1000}/.trajectory,{t,0,impacTime},PlotRange→All,AxesLabel→{"range,      km","altitude,
km"},AxesOrigin→{0,0}]
```

Now that the trajectory integration was successful, next plot the mass along the trajectory path

```
Plot[m[t]/.trajectory,{t,0,impacTime},PlotRange→All,AxesLabel→{"time, sec","mass, kg"}]

ParametricPlot[{m[t],z[t]/1000}/.trajectory,{t,0,impacTime},PlotRange→All,AxesLabel→{"mass, kg","altitude,
km"},AspectRatio→1]
```

The total mass fraction lost by ablation is:

```
finalmass:=m[impacTime]/.trajectory;
finalmass[[1]]

masslossFrac=(initMass-finalmass[[1]])/initMass

finalRadius=(3*finalmass[[1]]/(4*Pi*rhopart))^(1/3)

stagPressure[t_]:=0.5*rho[z[t]/.trajectory]*(v[t]/.trajectory)^2

Plot[stagPressure[t],{t,0,impacTime},PlotRange→All]

ParametricPlot[{0.5*rho[z[t]]*v[t]^2/10^5,z[t]/1000}/.trajectory,{t,0,impacTime},PlotRange→{{0,5*10^2},{0,30}},Axe
sLabel→{"stagnation pressure, bar","altitude, km"},AspectRatio→1]

ParametricPlot[{cdrag[renum[v[t],z[t],m[t]],mach[v[t]]],z[t]/1000}/.trajectory,{t,0,impacTime},AxesLabel→{"drag
coefficient","altitude, km"},AspectRatio→1]

ParametricPlot[{gfunc[renum[v[t],z[t],m[t]]],z[t]/1000}/.trajectory,{t,0,impacTime},AxesLabel→{"gfunc","altitude,
km"},AspectRatio→1]

ParametricPlot[{hfunc[mach[v[t]]],z[t]/1000}/.trajectory,{t,0,impacTime},AxesLabel→{"hfunc","altitude,
km"},AspectRatio→1]

ParametricPlot[{renum[v[t],z[t],m[t]],z[t]/1000}/.trajectory,{t,0,impacTime},AxesLabel→{"reynolds  number","altitude,
km"},AspectRatio→1,PlotRange→All]

ParametricPlot[{mach[v[t]]/renum[v[t],z[t],m[t]],z[t]/1000}/.trajectory,{t,0,impacTime},AxesLabel→{"knudsen
number","altitude, km"},AspectRatio→1,PlotRange→All]
```

At impact, the Knudsen number is very small:

```
mach[v[impacTime]]/renum[v[impacTime],z[impacTime],m[impacTime]]/.trajectory[[1]]
```

Bibliography

Batchelor, G. K. (1967). *An Introduction to Fluid Dynamics.* New York: Cambridge University Press.

Crowe, C. T. (1967). Drag Coefficient of Particles in a Rocket Nozzle. *American Institute of Aeronautics and Astronautics, 5* (5), 1021-1022.

Gattacceca, J., Lamali, A., Rochette, P., Boustie, M., & Berte, L. (2007). The Effects of Explosive-Driven Shocks on the Natural Remanent Magnetization and the Magnetic Properties of Rocks. *Physics of the Earth and Planetary Interiors, 162*, 85-98.

Gratz, A. J., Fisler, D. K., & Bohor, B. F. (1996). Distinguishing Shocked from Tectonically Deformed Quartz by the use of the SEM and Chemical Etching. *Earth and Planetary Science Letters, 142*, 513-521.

Holsapple, K. A. (1993). The Scaling of Impact Processes in Planetary Sciences. *Annual Review of Earth and Planetary Sciences, 21*, 333-373.

Holsapple, K. A., & Housen, K. R. (2007). A Crater and its Ejecta: An Interpretation of Deep Impact. *Icarus, 187*, 345-356.

Holsapple, K. A., & Schmidt, R. M. (1980). On the Scaling of Crater Dimensions 1. Explosive Processes. *Journal of Geophysical Research, 85* (B2), 7247-7256.

Holsapple, K. A., & Schmidt, R. M. (1982). On the Scaling of Crater Dimensions 2. Impact Processes. *Journal of Geophysical Research, 87* (B3), 1849-1870.

Holsapple, K. A., & Schmidt, R. M. (1987). Point Source Solutions and Coupling Parameters in Cratering Mechanics. *Journal of Geophysical Research, 92* (B7), 6350-6376.

Housen, K. R., & Holsapple, K. A. (2003). Impact Cratering on Porous Asteroids. *Icarus, 163*, 102-119.

Kenkmann, T., Artemieva, N. A., Wünnemann, K., Poelchau, M. H., Elbeshausen, D., & Núñez del Prado, H. (2009). The Carancas Meteorite Impact Crater, Peru: Geologic Surveying and Modeling of Crater Formation and Atmospheric Passage. *Meteoritics & Planetary Science, 44* (7), 985-1000.

Kohout, T., Kletetschka, G., Kobr, M., Pruner, P., & Wasilewski, P. J. (2004). The Influence of Terrestrial Processes on Meteorite Magnetic Records. *Physics and Chemistry of the Earth, 29*, 885-897.

Lanza, R., & Meloni, A. (2006). *The Earth's Magnetism: An Introduction for Geologists.* New York: Springer.

Loke, M. H. (2009, November 18). *Tutorial: 2-D and 3-D Electrical Imaging Surveys.* Retrieved November 24, 2009, from Geotomo Software:

http://www.geoelectrical.com/downloads.php (Lecture notes on 2D & 3D electrical imaging surveys)

Melosh, H. J., & Collins, G. S. (2005). Meteor Crater formed by low-velocity impact: The paucity of melted rock in this crater may be due to the striking projectile's speed. *Nature, 434*, 157.

Passey, Q. R., & Melosh, H. J. (1980). Effects of Atmospheric Breakup on Crater Field Formation. *Icarus, 42*, 211-233.

Petrovic, J. J. (2001). Review: Mechanical Properties of Meteorites and Their Constituents. *Journal of Materials Science, 36*, 1579-1583.

Steeples, D., & Miller, R. (1990). Seismic Reflection Methods Applied to Engineering, Environmental, and Groundwater Problems. In S. Ward (Ed.), *Geotechnical and Environmental Geophysics* (Vol. 1, pp. 1-30). Tulsa, Okla.: Society of Exploration Geophysicists.

Weibull, W. (1951). A Statistical Distribution Function of Wide Applicability. *Journal of Applied Mechanics, 18*, 140-147.

Wünnemann, K., Collins, G. S., & Melosh, H. J. (2006). A Strain-Based Porosity Model for use in Hydrocode Simulations of Impacts and Implications for Transient Crater Growth in Porous Targets. *Icarus, 180*, 514-527.